ENZYMATIC, STRUCTURAL AND BIOPHYSICAL CHARACTERIZATION OF A SINGLE DOMAIN ANTIBODY (VHH) SELECTIVELY AND TIGHTLY INHIBITING NEUTROPHIL ELASTASE AND EXHIBITING FAVORABLE DEVELOPABILITY PROPERTIES

Paola Redeghieri[1], Joël Moray[1], Frédéric Kerff[2], Sophie Gohy[3,4], Teresinha Leal[5], Serge Muyldermans[6], Rita Vanbever[7], Francisco Javier Morales-Yánez[1#] and Mireille Dumoulin[1#]

[1]Nano-antibodies to Explore Protein Structure and Functions (NEPTUNS), Centre for Protein Engineering, InBios, Department of Life Sciences, University of Liège, Liège, Belgium; [2]Biological Macromolecule Crystallography, Centre for Protein Engineering, InBios, Department of Life Sciences, University of Liège, Liège, Belgium; [3]Department of Pneumology, ENT and Dermatology, Institute of Experimental and Clinical Research (IREC), Université Catholique de Louvain, Brussels, Belgium; [4]Cystic Fibrosis Reference Centre, Cliniques Universitaires Saint-Luc, Brussels, Belgium; [5]Louvain Center for Toxicology and Applied Pharmacology (LTAP), Institute of Experimental and Clinical Research (IREC), Université Catholique de Louvain, Brussels, Belgium; [6]Laboratory of Cellular and Molecular Immunology, Vrije Universiteit Brussel, Brussels, Belgium; [7]Louvain Drug Research Institute (LDRI), Université Catholique de Louvain, Brussels, Belgium.

[#]Equal contributors.

Corresponding author: Mireille Dumoulin (mdumoulin@uliege.be). Nano-antibodies to Explore Protein Structure and Functions (NEPTUNS), Centre for Protein Engineering, InBios, Department of Life Sciences, University of Liège, Quartier Agora, Allée du 6 Août, 13, 4000 Liège (Sart-Tilman), Belgium. Tel: +32(0)43663546, Fax: +32(0)43663396

Running title: A VHH inhibiting neutrophil elastase

Total number of manuscript pages: 57

Supplementary material pages: 16

Tables: 1 (+ 1 in supplementary material)

Figures: 7 (+ 13 in supplementary material)

Description of supplementary material including filenames: one file comprising 13 figures with a description for every figure and additional information (material and methods, comments) for some figures, a table and an equation.

Abstract

Human neutrophil elastase (hNE), a serine protease released by neutrophils during inflammation, plays a major role in the pathophysiology of several conditions especially in inflammatory lung diseases. Its inhibition constitutes, therefore, a promising therapeutic strategy to combat these diseases. In this work, we characterized the *in vitro* properties of a VHH (i.e., the antigen binding domain of camelid heavy chain-only antibodies), referred to as NbE201. This VHH is able to inhibit tightly, selectively and competitively both human and murine elastases with the inhibition constants (K_i) of 4.1 ± 0.9 nM and 36.8 ± 3.9 nM, respectively. The IC_{50} for the inhibition of the hydrolysis of elastin is in the same range to that of alpha-1 antitrypsin (i.e., the main endogenous inhibitor of hNE also used in the clinic) and 14 times better than that of Sivelestat (i.e., the 2nd clinically approved hNE inhibitor). The X-ray crystal structure of the NbE201-hNE complex reveals that the Complementarity Determining Regions CDR1 and CDR3 of the VHH bind into the substrate binding pocket of hNE and prevent the access to small or macromolecular substrates. They do not, however, bind deep enough into the pocket to be hydrolyzed. NbE201 is highly stable towards oxidation, deamidation and chemical or thermal denaturation. NbE201 is therefore likely to tolerate manufacturing processes during drug development. These results highlight the high potential of NbE201 as a (pre)clinical tool to diagnose and treat diseases associated with excessive hNE activity, and for fundamental research to better understand the role of hNE in these conditions.

Key words: VHHs, camelid antibody fragments, elastase inhibition, competitive inhibitory VHH, thermodynamic stability, thermal stability, chemical stability, stability towards oxidation, developability, serine protease, neutrophilic inflammatory diseases

A 50-75-word statement, written for a broader audience, outlining the importance and/or impact of the work presented in the manuscript

We show that NbE201, a single-domain camelid antibody fragment isolated from an immune library following the immunization of a llama with human neutrophil elastase, acts as a tight, competitive and specific inhibitor of both human and murine neutrophil elastases. Moreover, it exhibits a high stability towards heat and chemical denaturation, and chemical modifications. It has, therefore, a promising therapeutic value for all diseases associated with excessive elastase activity.

Graphical abstract

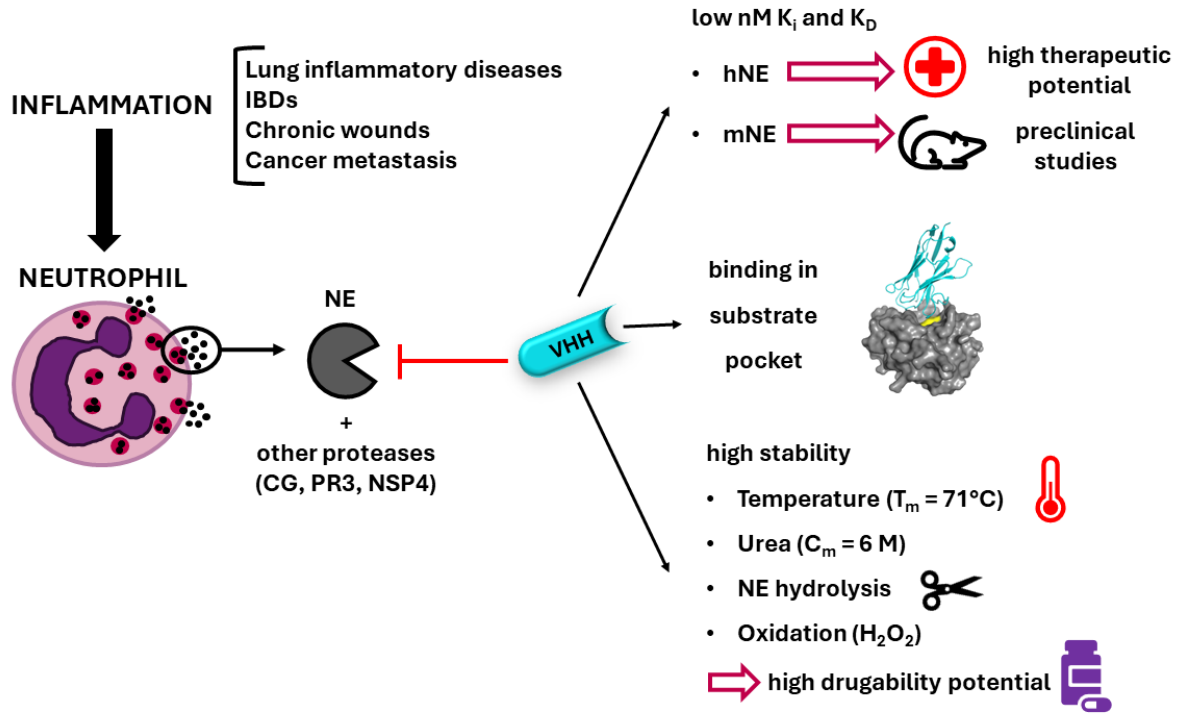

Abbreviations and symbols: AAT, alpha-1 antitrypsin; ALI, acute lung injury; ARDS, acute respiratory distress syndrome; AU, absorbance units; a.u., arbitrary units; BLI, bio-layer interferometry; BSA, bovine serum albumin; CDR, complementarity determining region; CF, cystic fibrosis; C_m, concentration of mid-transition; COPD, chronic obstructive pulmonary disease; D, denatured state; E, enzyme; $[E]_T$, total concentration in enzyme; Far UV-CD, far ultraviolet circular dichroism; F.I., fluorescence intensity; FR, framework region; F_{337}, fluorescence intensity at 337 nm; $\Delta G°_{NU(H20)}$, Gibbs free energy of unfolding; hCG, human cathepsin G; HEPES, N-(2-hydroxyethyl)piperazine-N-2-ethanesulfonic acid; hNE, human neutrophil elastase; hPR3, human proteinase 3; $[I]_T$, total concentration in inhibitor; IBDs, inflammatory bowel diseases; IC_{50}, half maximal inhibitory concentration; IMAC, immobilized metal ion affinity chromatography; IPTG, isopropyl β-D-thiogalactopyranoside; KB, kinetic buffer; K_D, equilibrium dissociation constant; K_i, constant of inhibition; K_i^{app}, apparent constant of inhibition, K_m, Michaelis constant; k_{on}, association rate constant; k_{off}, dissociation rate constant; m_{NU}, measure of the dependence of the Gibbs free energy between the native and denatured state on the denaturant concentration; mNE, murine neutrophil elastase; mPE, murine pancreatic elastase; N, native state; NE, neutrophil elastase; NETosis, neutrophil extracellular traps release; pNA, paranitroanilide; POC, point of care; pPE, porcine pancreatic elastase; RMSD, root-mean-square deviation; ROS, reactive oxygen species; S, substrate; SA, streptavidin; SLPI, secretory leucocyte proteinase inhibitor; T_m^{app}, apparent temperature of mid-transition; U, unfolded state; uPA, trypsin-like urokinase-type plasminogen activator; UV, ultra-visible; v_0, initial rate of hydrolysis; VHH, variable domain of heavy chain-only antibodies; v_i, initial rate of hydrolysis in the presence of inhibitor.

1 INTRODUCTION

Human neutrophil elastase (hNE) is a serine protease belonging to the chymotrypsin family (EC 3.4.21.37). It is a critical protease in immune response and host defense mechanisms in both physiological and disease-associated conditions. It is stored in the azurophilic granules of polymorphonuclear neutrophils and is released, at the site of inflammation, during neutrophil degranulation and neutrophil extracellular traps release (NETosis)[1]. This glycosylated protease is able to degrade critical proteins from the extracellular matrix such as elastin, collagen, fibronectin and laminins, and other extracellular proteins such as immunoglobulins[1,2]. Moreover, it also stimulates the release of inflammatory cytokines and the activation of other proteases[3,4,5]. Under physiological conditions, the amount of extracellular active hNE is tightly regulated, mainly by the antiproteases alpha-1 antitrypsin (AAT), secretory leucocyte proteinase inhibitor (SLPI) and elafin[1]. In several pathological conditions, this balance is, however, displaced towards excessive hNE which contributes to many inflammatory diseases. Uncontrolled hNE activity is associated, among others, with progressive destruction of tissues and loss of their associated functions and impaired immune system regulation[4]. These diseases comprise, but are not restricted to, chronic wounds[6,7], cancer metastasis[8,9,], artherosclerosis[10], psoriasis[11], inflammatory bowel diseases (IBDs)[12–14] and a series of lung-related diseases (e.g., cystic fibrosis (CF)[4], chronic obstructive pulmonary disease (COPD)[15], bronchiectasis[16], and more recently severe acute respiratory syndrome in SARS-Cov-2[17]).

In all these conditions, the inhibition of excessive hNE activity is expected to prevent or decrease its detrimental effects. Thus, extensive research is carried out to identify hNE inhibitors (small molecules, aptamers or protein-based). Small molecules that inhibit hNE have been

studied by major pharmaceutical companies[18,19]. However, only one of these molecules (Sivelestat) has been approved for clinical use for a very limited number of acute conditions (i.e., acute respiratory distress syndrome, ARDS, and acute lung injury, ALI) in Japan, South Korea, and more recently in China[20,21]. It has, however, not been approved by FDA due to controversial results on efficacy and safety[22,23,24]. The limited use of small inhibitory molecules is mostly due to their low efficacy in elastase inhibition, a lack of elastase selectivity and thereby a risk of side effects and a lack of stability *in vivo*[18,20]. Aptamers have been shown to inhibit hNE but none of them have undergone clinical trials[25]. As far as protein-based inhibitors are concerned, several AAT-based drugs are in clinical use to treat patients affected with AAT deficiency, they are however not used for any other of the diseases listed above. Thus, there is a significant unmet medical need to develop new highly efficient and specific inhibitors of hNE.

Monoclonal antibodies and engineered antibody fragments present the advantages of high affinity and target specificity and thereby fewer adverse events compared to small molecule drugs[26,27]. A few monoclonal antibodies and antibody fragments targeting elastase have been described and some of them exhibit inhibitory effects[28,29]. The half maximal inhibitory concentration (IC_{50}) for elastase, when available, is however in the µM range[29], and none of them has been envisioned for therapy. Due to their unique properties, VHHs, which are the antigen binding domains of camelid heavy-chain only antibodies, constitute a unique alternative to conventional monoclonal antibodies and their derived fragments to inhibit enzymes[30,31]. Despite their small size, the affinity and specificity of VHHs for their target is comparable to those of classical antibodies. Because of their small size, VHHs display a series of beneficial properties including high stability and solubility, economic production in *E. coli*, easy modification by genetic engineering, high tissue penetration and, most important for this work, an ability to target, via a long fingertip CDR3 (Complementarity Determining Region

3), cryptic epitopes generally inaccessible to conventional antibodies such as the active site of enzymes[32]. Several VHHs inhibiting proteases have been described[33–35]. Thus, VHHs constitute excellent candidates to generate new elastase inhibitors.

In this study, we characterize in detail the *in vitro* properties of NbE201, a VHH retrieved after phage display from an immune library constructed from the blood of a llama immunized with hNE. NbE201 acts as a tight, competitive and specific inhibitor of neutrophil elastase from both human and murine origins. The crystal structure of the complex between hNE and NbE201 demonstrated the essential role of the CDR1 and CDR3 antigen binding loops of the VHH to interact with the substrate binding pocket of the enzyme. They do not, however, enter sufficiently deep into the pocket to be hydrolyzed. NbE201 exhibits high stability towards chemical or heat denaturation, and towards deamidation and oxidation. Altogether, these results highlight the high potential of NbE201 as a (pre)clinical agent to diagnose and treat diseases associated with excessive hNE activity as well as for fundamental research to elicit the exact involvement of hNE in these diseases.

2 RESULTS

2.1 Production and purification of NbE201

NbE201 was selected by directional sandwich phage display panning in solution from an immune library at the ALPANANO platform of the Centre for Protein Engineering (ULiège). Briefly, hNE was captured on streptavidin (SA)-coated magnetic beads *via* the binding of a biotinylated anti-hNE VHH that binds far away from the active site of the enzyme, and three rounds of phage display selection were performed. The details of the selection will be published elsewhere (F. Morales-Yànez *et al*., in preparation). NbE201 was expressed as a

soluble protein into the periplasm of *E. coli* WK6 cells, and purified to homogeneity by an immobilized metal ion affinity chromatography (IMAC) via its C-terminal His_6-Tag (Figure SI1A,B), followed by buffer exchange *via* gel filtration (Figure SI1C,D). Several independent batches were produced and the best practice recommendation established by the ARBRE-MOBIEU and P4EU networks[36] was used to assess their quality and to establish batch-to-batch consistency. In each lot, the purity of NbE201 was higher than 98% as judged by SDS-PAGE analysis (Figure SI1D). Its integrity was confirmed by mass spectrometry which revealed one major species corresponding to a molecular mass comprised between 14331 and 14334 Da depending on the lot of production. Within the error limit, this mass is identical with the theoretical one calculated from the sequence using the ProtParam tool from Expasy, 14333.03 Da. The UV absorbance spectrum (Figure SI1E) demonstrated the absence of aggregates ($A_{310nm} = 0$) and of nucleic acid contamination (i.e., ratio $A_{280nm}/A_{260nm} > 2$). The far UV circular dichroism (CD) spectrum of NbE201 is typical of that of immunoglobulin domains[37] (Figure SI2, in black). In the presence of 9 M urea or at high temperatures, the spectra are characteristic of a random coil structure (Figure SI2, in red) indicating that NbE201 is fully denatured under these conditions. The intrinsic fluorescence spectrum of NbE201 in the native state exhibits a maximum at 351 nm (Figure SI3, in black) indicating that at least one of the three tryptophan residues is exposed to the solvent, which is in agreement with previous observations with other VHHs[37]. In the presence of 9 M urea or at high temperatures, the spectrum is shifted towards higher wavelengths, indicating denaturation (Figure SI3, in red). Altogether, these observations are indicative that NbE201 was purified as a natively folded protein.

2.2 NbE201 is a tight inhibitor of hNE

Inhibition of the hydrolysis of a small synthetic substrate. The residual activity of hNE towards the hydrolysis of N-Succinyl-Ala-Ala-Ala-paraNitroAnilide in the presence of different concentrations of NbE201 was determined from the initial rate of substrate hydrolysis (Figure 1A). The experiment was repeated with three different lots of production of NbE201 and the average IC_{50} is 38.3 ± 3.3 nM. Thus, the activity of hNE is significantly inhibited in the presence of a VHH concentration similar to the total enzyme concentration (i.e., 50 nM). This observation indicates that NbE201 acts as a tight binding inhibitor[38]. Similar inhibition was observed whether NbE201 was preincubated or not with hNE for 15 min before the addition of the substrate. Moreover, there was no curvature, at the initial time points, in the curve showing A_{410nm} as a function of time, whether the experiment was carried out into a microplate format (deadtime of the experiment of 100 s) or in a 1.5 mL cell (deadtime of the experiment of 14 s) indicating that the equilibrium between the enzyme, substrate and NbE201 is reached within seconds.

The K_i value was determined using the Morrison's equation[38] (Eq 1) established for tight binders and defined as follows:

$$\frac{v_i}{v_o} = 1 - \frac{([E]_T+[I]_T+K_i^{app}) - \sqrt{([E]_T+[I]_T+K_i^{app})^2 - 4[E]_T[I]_T}}{2[E]_T} \qquad \text{(Eq 1)}$$

with v_i and v_0 as the initial rate measured in the presence and in the absence of inhibitor, respectively; $[E]_T$, is the total enzyme concentration, $[I]_T$, is the total inhibitor concentration and K_i^{app}, is the apparent constant of inhibition.

As detailed below, NbE201 is a competitive inhibitor, thus $K_i^{app} = K_i(1 + \frac{[S]}{K_m})$ (Eq 2) with K_i the constant of inhibition, [S] the concentration in substrate and K_m the Michaelis constant[38]. The K_m, derived using the Hanes-Woolf linearization method, is equal to 1.4 mM (Figure

SI4A,B). The average K_i, derived from the individual fitting of the three experimental curves v_i/v_0 as function of the concentration of NbE201 using Eq 1 is equal to 4.1 ± 0.9 nM.

The hNE inhibition for the hydrolysis of N-Succinyl-Ala-Ala-Ala-paraNitroAnilide by AAT and Sivelestat has also been investigated for comparison (Figure 1B). The IC_{50} are, respectively: 22.0 ± 5.3 nM and 71.3 ± 9.0 nM. The IC_{50} for AAT is equal within the error limit to the half of the concentration of hNE (i.e., 25 nM) which is expected given that AAT is a nearly irreversible covalent inhibitor of hNE (Eq SI1) characterized by a very high association rate constant (at least 10^7 $M^{-1}s^{-1}$) and a very slow dissociation rate constant (no more than $2 \cdot 10^{-6}$ s^{-1}) (K_D in fM range)[39]. The IC_{50} of NbE201 is in the same range as that of AAT and Sivelestat.

Inhibition of the hydrolysis of elastin, a natural substrate of hNE. To better evaluate the clinical inhibitory potential of NbE201, measurements of hNE hydrolysis of one of its physiological substrates, elastin, were carried out in the presence of NbE201, AAT and Sivelestat (Figure 1C). hNE and Elastin-CongoRed were used at concentrations of 132 nM and 1 $mg \cdot mL^{-1}$, respectively. The IC_{50} are: 480 ± 60 nM, 120 ± 4 nM and 6700 ± 1700 nM for NbE201, AAT and Sivelestat, respectively.

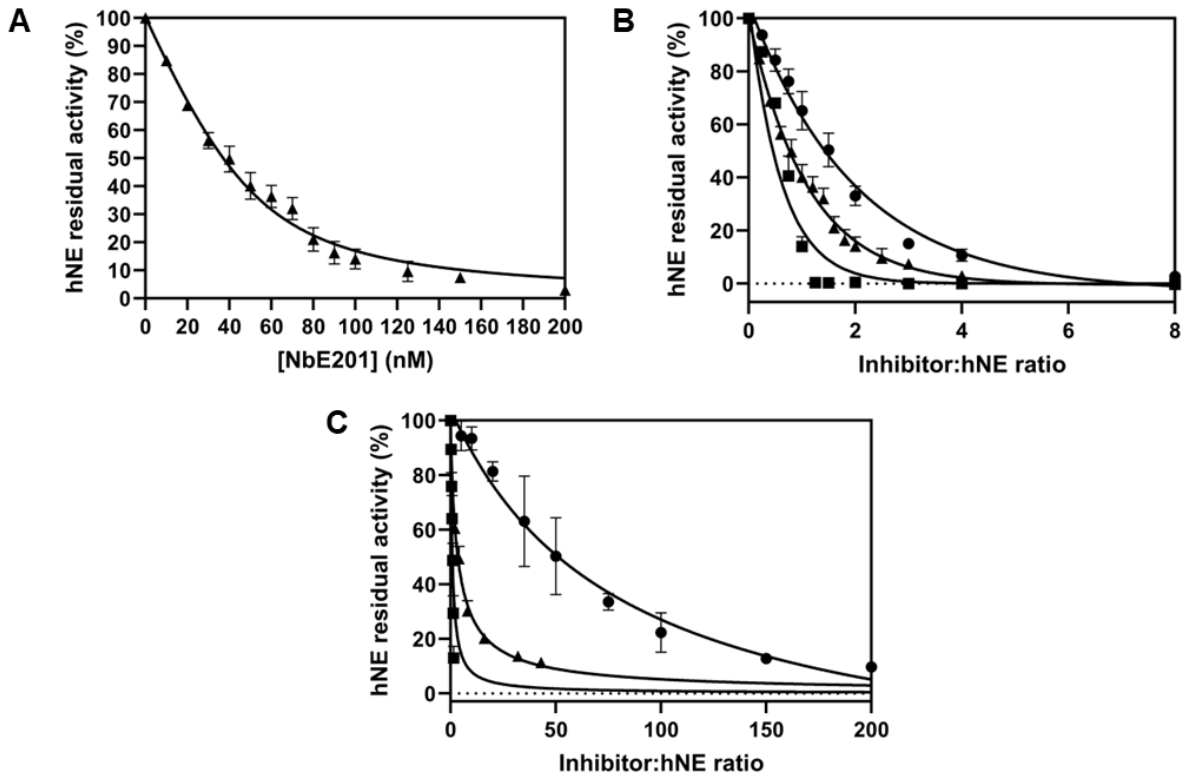

Figure 1. **Curves of hNE residual activity (in percentage)**. Hydrolysis of the small chromogenic substrate N-Succinyl-Ala-Ala-Ala-paraNitroAnilide at A) different NbE201 concentrations (the experiments were carried out in triplicate with three different lots of production, N=3), and B) in the presence of different concentrations of (■) AAT (N=3) and (●) Sivelestat (N=3) (the data in the presence of NbE201 from panel A are also shown for comparison, ▲). C) Hydrolysis of elastin at different [inhibitor]/[hNE] ratios: (■) AAT (N=3), (▲) NbE201 (N=3) and (●) Sivelestat (N=3). A,B,C) The displayed dots are the average of the independent measurements and the error bars correspond to the SD.

2.3 NbE201 binds hNE with high affinity

Quantitative binding measurements were performed to measure the kinetic (k_{on}, association rate and k_{off}, dissociation rate) and equilibrium (K_D, equilibrium dissociation) constants using bio-layer interferometry (BLI) (Figure 2A). The global fit of the kinetics obtained with 5

different concentrations of hNE was carried out with the 1:1 binding model. As shown on Figure 2A, at high concentrations in hNE, the fit deviates from experimental data especially during the dissociation phase which is diphasic. This could be indicative of a mass transport effect. Indeed, the data are better fitted with a 1:1 model with mass transport (see Figure SI5A). This mass transport was observed despite the optimization of the assay by immobilizing the lowest amount of VHH on the biosensor (about 0.12 nm signal) allowing a detectable signal for the association/dissociation phases to be observed. The kinetics and equilibrium constants characterizing the binding and derived from the 1:1 binding model are reported in Figure 2B. The binding is, in any case, characterized by a very fast association rate constant ($2.2 \pm 0.9 \cdot 10^6$ M^{-1} s^{-1}), which likely causes a rebinding effect of the hNE on the immobilized NbE201 during the dissociation phase, and a k_{off} of $4.8 \pm 2.8 \cdot 10^{-3}$ s^{-1}. Therefore, due to this mass transport limitation, both k_{on} and k_{off} values are likely to be underestimated. However, the value of the K_D obtained is in rather good agreement with the K_i derived from the enzymatic assay, which indicates that the underestimation of the rate constants and and K_D remains minor.

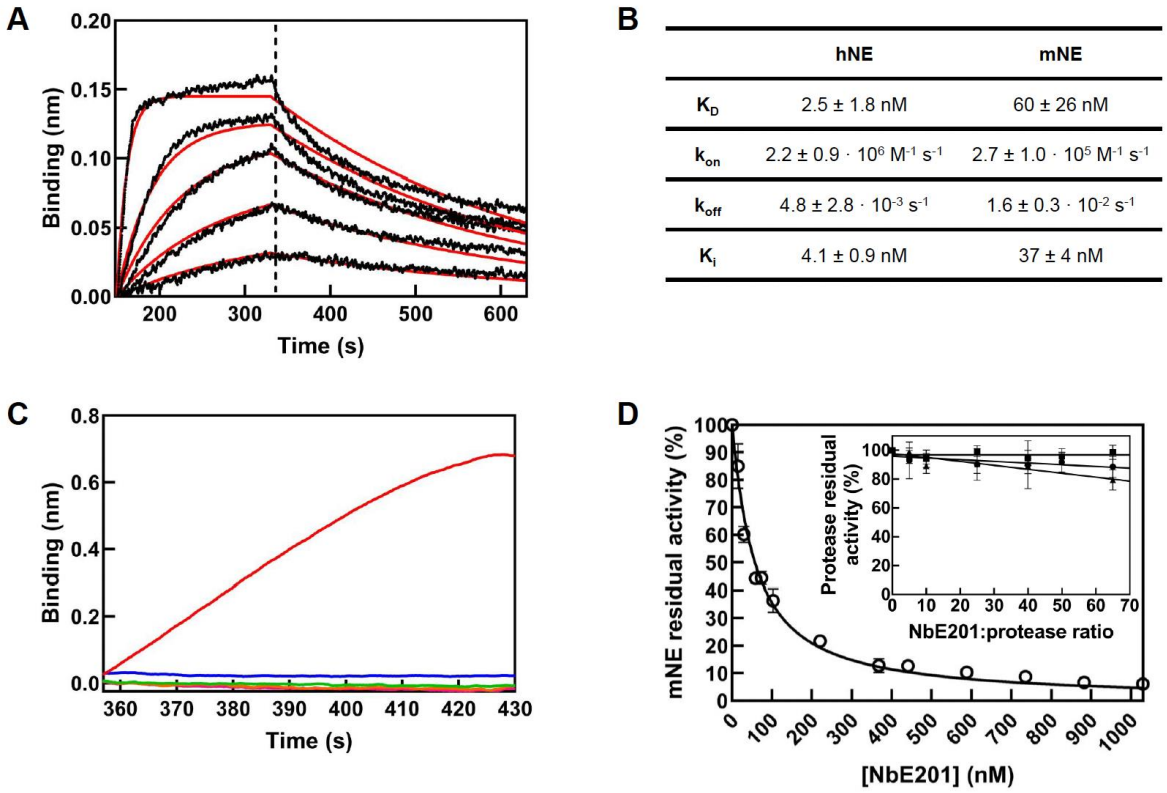

	hNE	mNE
K_D	2.5 ± 1.8 nM	60 ± 26 nM
k_{on}	2.2 ± 0.9 · 10^6 M^{-1} s^{-1}	2.7 ± 1.0 · 10^5 M^{-1} s^{-1}
k_{off}	4.8 ± 2.8 · 10^{-3} s^{-1}	1.6 ± 0.3 · 10^{-2} s^{-1}
K_i	4.1 ± 0.9 nM	37 ± 4 nM

Figure 2. **Affinity and specificity of NbE201 for neutrophil elastase**. (A) Representative measurement of the NbE201 affinity for hNE by BLI. A vertical dashed line divides the association step from the dissociation step. The kinetics of association and dissociation between hNE at different concentrations (analyte), and NbE201 immobilized on the sensor (ligand) are shown. Each curve (in black) represents datathe binding ($\Delta\lambda$ in nm) referring to a single concentration of hNE used: 25 nM, 6.25 nM, 3.12 nM, 1.56 nM and 0.75 nM (from top to bottom). In red, is represented the fitting of the data from which the K_D value and kinetic parameters were derived. Data were fitted globally accordingly to a 1:1 binding model by using the Data Analysis Octet Software Version 10.0 (Sartorius). (B) K_D, k_{on} and k_{off} values describing the binding between NbE201 and hNE or mNE. Independent replicates of the experiment were carried out (N=3) and the mean (± SD) of the kinetics parameters measured are indicated. The K_i determined from enzymatic assay for hNE (N=3) and for mNE (N=5) is

also shown. The error for the K_D were calculate using Eq 3 (Material and methods, section 5.4). (C) Sensorgrams of the association between NbE201 and different serine proteases: hNE (red), hCG (green), hPR3 (orange), mPE (blue) and pPE (pink). hNE is the only proteases between the ones tested that binds to NbE201 immobilized on the sensor. The other proteases (hCG, hPR3, mPE and pPE) do not show any binding signal. (D) Curve of residual mNE activity (in percentage) at different NbE201 concentrations (○) (N=5). In the insert, the residual activity of several serine proteases in the presence of different ratios of NbE201:protease is shown. The proteases tested are: hPR3 (▲), hCG (■) and pPE (●). The experiments were carried out in triplicates (N=3). The displayed points are the average of the independent measurements and the error bars show the SD.

2.4 Specificity of NbE201 for NE

Binding and inhibition of other serine proteases. The ability of NbE201 to bind other serine proteases was evaluated with a BLI assay in the presence of four different serine proteases at a 50 nM concentration: human cathepsin G (hCG), human proteinase 3 (hPR3), mice pancreatic elastase (mPE) and porcine pancreatic elastase (pPE). The sequence identity between these proteases and hNE are respectively: 36.2%, 54.7%, 37.1% and 39.6%. An association signal is observed only when NbE201 is in contact with hNE (which was used as positive control, Figure 2C), which means that NbE201 does not significantly bind to any of the four other enzymes. The ability of NbE201 to inhibit hPR3, hCG and pPE was investigated using small chromogenic substrates (Figure 2D, insert). The results obtained indicate that NbE201 does not inhibit hCG. It can, however, inhibit hPR3 and pPE, but with a very low efficiency compared to the inhibition of hNE: 20% of inhibition of hPR3 at a NbE201:enzyme ratio of 65 and 10% of inhibition of pPE at a NbE201:enzyme ratio of 65 (IC_{50} >> 3.2 µM for

both enzymes). The absence of binding of NbE201 to hPR3 and pPE in BLI experiment is probably due to a NbE201:enzyme ratio too low to allow detectable interactions. Altogether these results indicate that NbE201 is highly specific for hNE.

NbE201 binds to and inhibits murine NE. NbE201 significantly inhibits murine neutrophil elastase activity (mNE, 76.7 % of sequence identity with hNE) as shown in Figure 2D. The IC_{50} is 49.4 ± 6.6 nM for the hydrolysis of MeOSuc-Ala-Ala-Pro-Val-AMC while the mNE concentration is 14.7 nM, thus NbE201 also act as a tight inhibitor for mNE ($IC_{50} < 10[mNE]$)[38]. No direct comparison can be made with the IC_{50} obtained with hNE since the experimental conditions used (including the substrate) are different. The K_m, determined using the Hanes-Woolf linearization method (Figure SI4C,D), is equal to 0.478 ± 0.044 mM. The K_i for mNE derived using Morrison's equation is 37± 4 nM, which is about 10 times higher than the K_i calculated for hNE. The affinity between NbE201 and mNE was measured by BLI (Figure SI5B) and the kinetics and equilibrium binding parameters are reported in Figure 2B. The association rate constant for the interaction between Nb201 and mNE is about 8 times lower than that observed for hNE, and the dissociation rate constant is about 3 times higher. The affinity between NbE201 and mNE of 60.0 ± 26.0 nM, which is in accordance with the K_i value measured. Note that as shown in Figure SI5C,D in supplementary material, the lower affinity for mNE is not due to the differences in the buffer conditions used for the two enzymes.

2.5 NbE201 is a competitive inhibitor of NE and binds into its active site

Competitive binding with active site ligands monitored by BLI. To determine if NbE201 binds into or near the active site of hNE, competitive binding experiments were performed with molecules known to bind into the hNE active site. NbE201 was immobilized on a biosensor and put in contact with a hNE solution preincubated or not with saturating concentrations of

inhibitors binding to hNE active site. AAT was first tested. Figure 3C (in blue) shows that hNE in complex with AAT does not bind to NbE201, suggesting that NbE201 bind into the active site of the enzyme. Within the hNE-AAT complex, the structure of both proteins differ from that of their free form as a result of conformational changes[40]. Thus, the absence of binding of the hNE-AAT preformed complex to NbE201 could result from the fact that NbE201 epitope is not present anymore on the surface of hNE due to this conformational reorganization. In order to further test this hypothesis, two other inhibitors known to bind hNE active site were tested: (i) MeOSuc-Ala-Ala-Pro-Val-CMK which is a small molecule inhibitor covalently binding in hNE active site without inducing a conformational change[41] and (ii) cAb-H7S-Nter-P1, a chimeric VHH designed for this purpose. cAb-H7S-Nter-P1 is composed of a VHH (cAb-H7S) which does not bind to hNE fused at its N-terminal to an inhibitory peptide (P1) that binds hNE active site non-covalently[42]. Figure 3C shows that, when preincubated with saturating concentrations of these two inhibitors, hNE is unable to bind to NbE201. While the competition between NbE201 and AAT or cAb-H7S-Nter-P1 could result from steric hindrance effects (i.e. NbE201 binds close to the active site preventing the binding of AAT or cAb-H7S-Nter-P1), the competition with MeOSuc-Ala-Ala-Pro-Val-CMK strongly suggests that NbE201 binds into the active site of the enzyme.

NbE201 behaves as a strong inhibitor, not as a substrate. To investigate if NbE201 is a very poor substrate or an inhibitor, its stability towards hNE proteolytic activity was tested for 14 days and was assessed by SDS-PAGE (Figure 3A,B). The intensity of the VHH band does not significantly decrease over time and is similar to that observed with an incubation in the absence of hNE. This observation suggests that the NbE201 is not hydrolysed by the enzyme. The experiment was limited to 14 days because the residual activity of hNE after this period

is close to zero (Figure 3B). These results indicate that NbE201 behaves as a strong inhibitor and not as a very poor substrate.

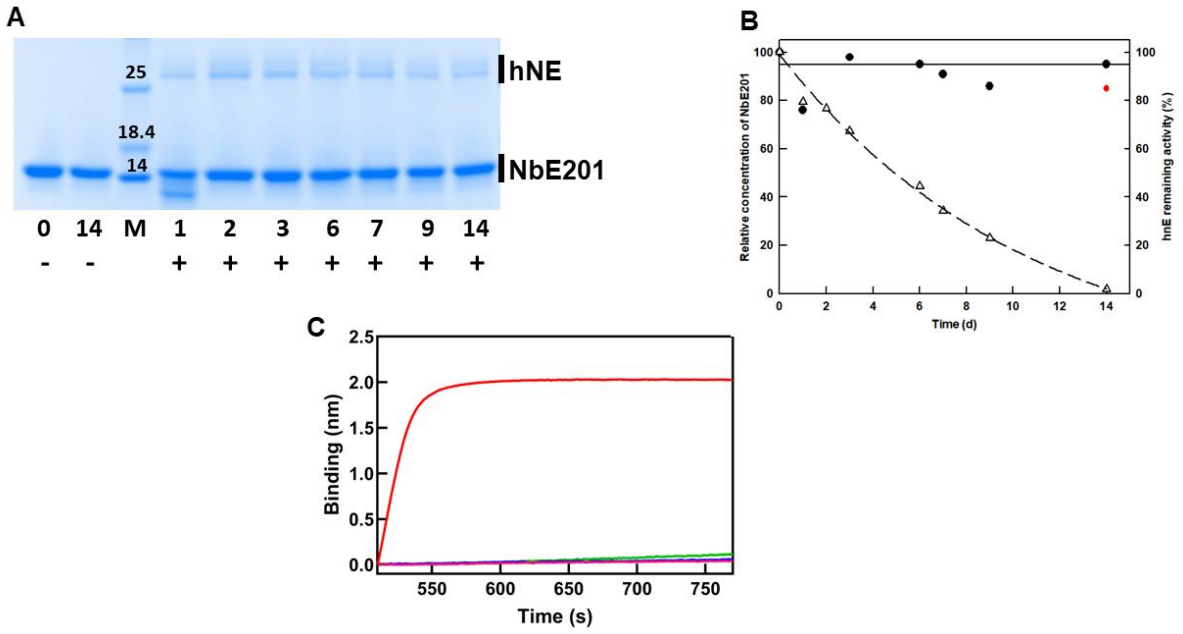

Figure 3. **A,B) Stability of NbE201 towards hNE activity and C) NbE201 competitive binding for hNE active site**. A) SDS-PAGE analysis of the complex (under reducing conditions). The number below the gel indicates the time in days during which NbE201 was incubated, at 37°C, in the presence (+) or absence (-) of hNE. M, Molecular size marker in kDa. B) Relative concentration in NbE201 derived from panel (A) in the presence (●) or absence (●) of hNE (left axis) and remaining activity of hNE in percentage versus time of incubation in days (△, right axis). C) Competitive binding between NbE201 and hNE complexed with a series of known inhibitors monitored by BLI. The biotinylated NbE201 was first immobilized on SA sensors. In the association step, the sensors were immersed into a solution of hNE (in red) or hNE complexed with AAT (in blue), cAb-H7S-Nter-P1 (in green) or MeOSuc-Ala-Ala-Pro-Val-CMK (in pink). The signal for MeOSuc-Ala-Ala-Pro-Val-CMK and AAT are superimposed.

X-ray structure of free NbE201 and NbE201-hNE complex. The NbE201-hNE complex crystallized in the $P2_12_12_1$ space group with a single complex in the asymmetric unit. The structure was solved by molecular replacement to 2.3 Å resolution with R_{work} and R_{free} values of 22.4% and 27.1% respectively (Table SI1).

This structure includes all residues from hNE (I16 to Q243, numbered according to the chymotrypsinogen scheme), except for amino acids R147 and N148 which were not defined in the electron density, and all amino acids of NbE201 (Q1 to S123 according to the FASTA numbering) (Figure 4A,B). hNE adopts the typical chymotrypsin fold essentially made of two β-barrels (where each one is composed by six anti-parallel β-sheets) and a C-terminal α-helix (Figure 4B, in grey). The catalytic triad (H57, D102 and S195) is formed by the interactions from both β-barrels. The two glycosylation sites NAG-NAG-FUC were found at positions N109 and N204. The interaction surface between the two proteins covers 885 $Å^2$ according to PiSA (https://www.ebi.ac.uk/msd-srv/prot_int/pistart.html).

To investigate whether the binding of NbE201 induces conformational changes into the structure of hNE, the RMSD (root-mean-square deviation) for the Cα of hNE within the complex (216 atoms) and the free hNE (PDB entry 3Q76, 218 atoms) was calculated (Figure SI6). With an RMSD of 0.42 Å (214 to 214 atoms aligned), it is clear that no structural reorganization of hNE occurs upon binding of the VHH via allosteric effects.

The 12 residues of NbE201 in interaction with hNE belong to the CDR1 (3 residues out of 8, GRT**IS**L**Y**R), the CDR2 (1 residue out of 8, IN**W**SGDMT), the CDR3 (7 residues out of 16, TAD**PKLL**PLA**D**SS**Y**G**Y**) and the first framework region (FR1) (i.e., residue **V2**). These interactions include eight hydrogen bonds (one mediated by a water molecule) and three hydrophobic clusters (Table 1, Figure 4C-F).

Type of interaction	**NbE201**	**hNE**	**Distance (Å)**	**Figure 4 panel**
Polar	V2 N (FR1)	V97 O (90s loop)	3.0	C
Polar	S30 N (CDR1)	V216 O (S1)	2.9	D
Polar	S30 OH (CDR1)	G219 N (220s loop)	2.7	D
Polar (via H_2O)	P100 O (CDR3)	S195 OH (catalytic triad), G193 N (oxyanion hole)	3.4 (2.9, 3.1)	E
Polar	K101 NZ (CDR3)	A60 O (60s loop)	2.9	E
Polar	D107 OD1 (CDR3)	R36 NH1 (37s loop)	3.3	F
Polar	Y110 O (CDR3)	N61 ND2 (S1')	2.8	F
Polar	Y112 OH (CDR3)	P96 O (90s loop)	2.9	F
Hydrophobic cluster 1	V2 (FR1), I29 (CDR1)	L99B (90s loop), F215 (S2)		C
Hydrophobic cluster 2	Y32 (CDR1), W53 (CDR2), L102 (CDR3)	L143 (S2'), I151 (S2'), F192 (S1)		D

Hydrophobic cluster 3	P100, K101, L103 (CDR3)	L35 (37s loop), F41, C42 (S2'), H57 (catalytic triad and S2), C58 (S2), V62 (60s loop)	E

Table 1. **Table of interactions between NbE201 and hNE**. For NbE201, the region on the VHH to which the amino acids belong to is indicated in brackets. For hNE, the region of interaction on the enzyme (i.e., substrate pocket, oxyanion hole, catalytic triad or specificity loop) is also indicated in bracket. The distances between the interacting atoms have been calculated with PyMOL software. The number of figure panel showing these interactions is indicated.

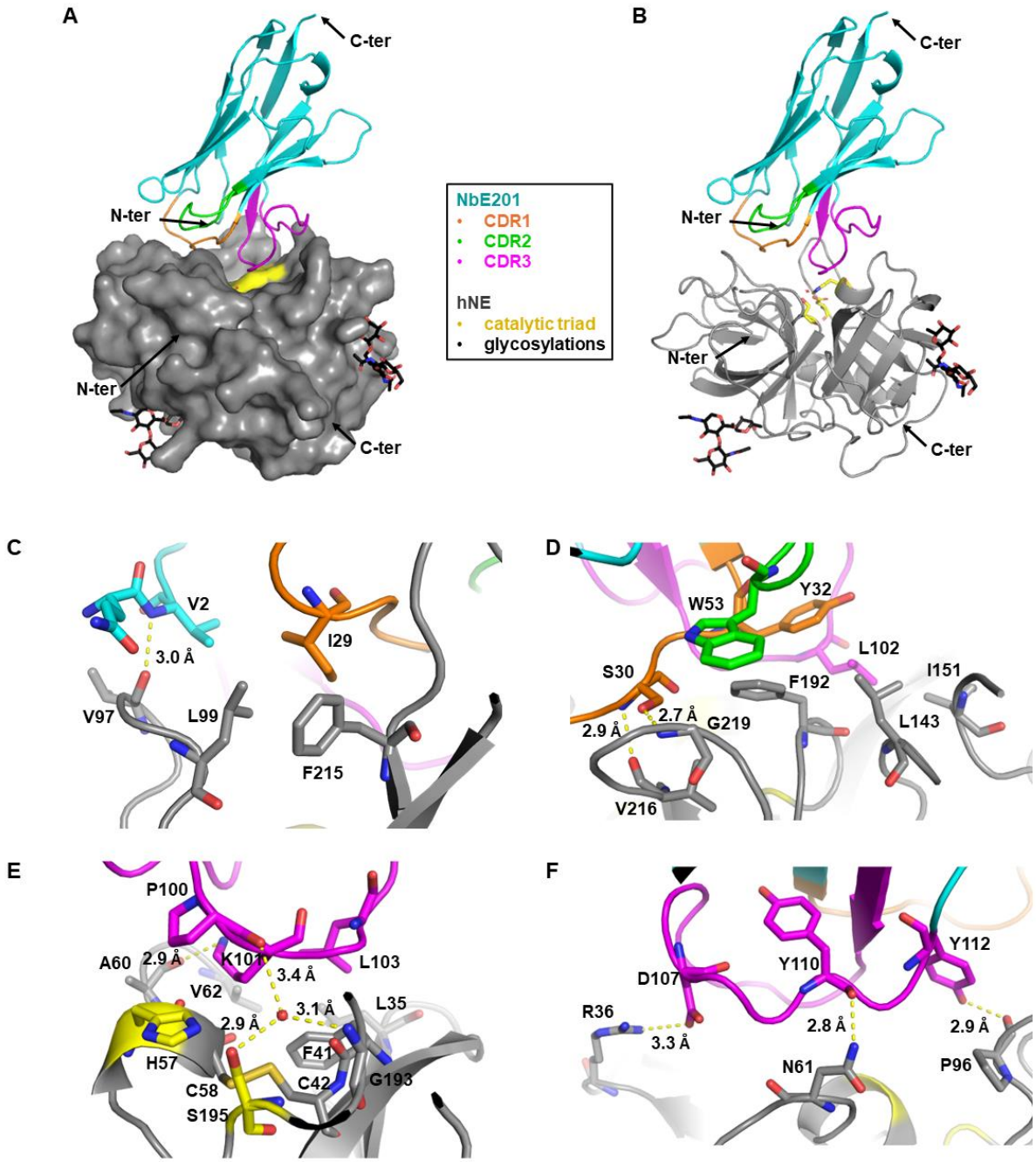

Figure 4. **3D structure of the NbE201:hNE complex solved by X-ray crystallography**. A) hNE is shown as a grey surface and NbE201 in cyan as a cartoon. The CDR1, CDR2 and CDR3 regions are depicted in orange, green and magenta respectively. The glycosylation sites NAG-NAG-FUC at positions N109 and N204 of hNE are shown as black sticks. The catalytic triad of hNE is coloured in yellow. B) The same structure is represented in cartoon style with the catalytic triad of the enzyme coloured in yellow sticks. C-F) Detailed representation of the interactions

between hNE and NbE201. The colour code is similar to that in panels A&B. H-bonds distances are represented as yellow dotted lines. The coordinated molecule of water (panel E) is shown as a red sphere.

The structure of the VHH alone was determined at a resolution of 1.8 Å (Figure SI7). The crystal belongs to the $P2_12_12_1$ group (Table SI1). The asymmetric unit contains four molecules of NbE201. The structure of NbE201 was superimposed to that of the VHH in complex with hNE. The RMSD on the Cα, calculated with PyMOL, is 0.64 ± 0.02 Å (mean of the superimposition of the four molecules of NbE201 found in the asymmetric unit, with the complex NbE201-hNE) and no structural differences are seen (Figure SI8). Thus, NbE201 does not experience significant conformational changes upon binding to hNE.

2.6 NbE201 is highly stable

Stability of NbE201 towards urea-induced unfolding. The thermodynamic stability of NbE201 was investigated by urea-induced unfolding monitored by intrinsic fluorescence (the wavelength corresponding to the maximum in fluorescence intensity, λ_{max} and fluorescence intensity at 337 nm, F_{337nm}) and far UV-CD (signal at 207 nm). In both cases, a single transition was obtained suggesting that both the tertiary and secondary structures unfold cooperatively following a two-state model (N↔U) (Figure 5A,B). The reversibility of the denaturation, after dilution of the urea concentration was established both by intrinsic fluorescence (Figure SI9A) and the ability to inhibit hNE (Figure SI9B). The results of fluorescence experiments showed that the unfolding and refolding processes of NbE201 are superimposable throughout the transition (Figure SI9). Moreover, NbE201 unfolded into 7.6 M urea and refolded into 0.76 M recovered it full ability to inhibit hNE. NbE201 unfolding in urea is therefore fully structurally and functionally reversible. Moreover, the coincidence of the transition curves obtained by

intrinsic fluorescence and far UV-CD measurements after normalization demonstrates that secondary and tertiary structures are unfolded concomitantly (Figure 5C). Thus, the denaturation of the protein can be described by an apparent cooperative two-state model (N ⇌ U), where only the native and unfolded states are significantly populated. Values of the thermodynamic parameters were computed from the raw transition monitored by the three parameters ($\lambda_{max,}$ F_{337nm} and far UV-CD at 207 nm, Figure 5A,B) assuming a simple two-state model and Eq 4 (Figure 5F).

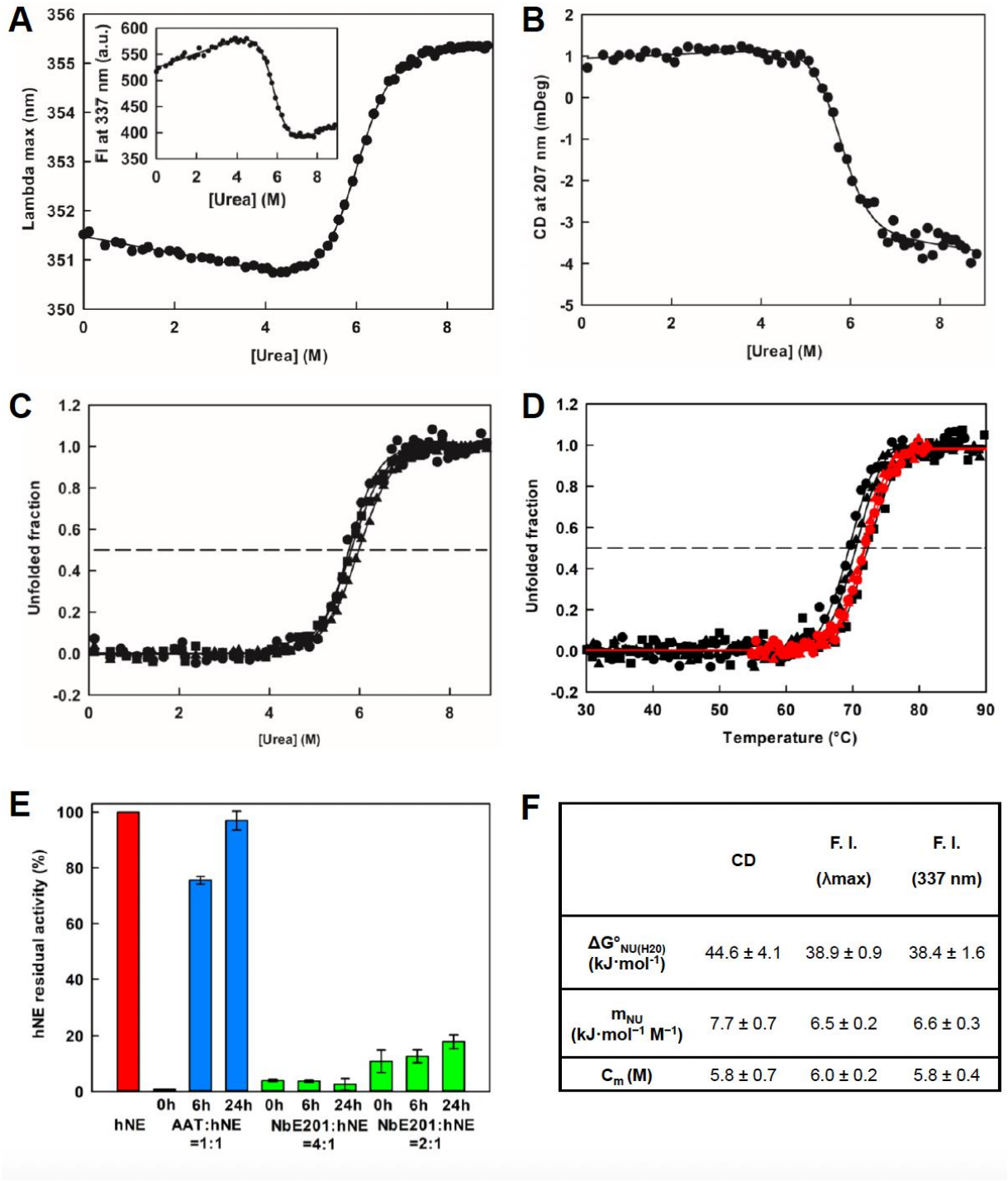

	CD	F. I. (λmax)	F. I. (337 nm)
$\Delta G°_{NU(H20)}$ (kJ·mol^{-1})	44.6 ± 4.1	38.9 ± 0.9	38.4 ± 1.6
m_{NU} (kJ·mol^{-1} M^{-1})	7.7 ± 0.7	6.5 ± 0.2	6.6 ± 0.3
C_m (M)	5.8 ± 0.7	6.0 ± 0.2	5.8 ± 0.4

Figure 5. **Stability of NbE201 towards chemical and heat-induced denaturation**. A,B) Urea-induced unfolding transitions of NbE201 monitored by intrinsic fluorescence and far UV-CD. The transitions were monitored by: A) changes in the wavelength of maximal fluorescence intensity (Lambda max), (A, insert) changes in fluorescence emission intensity at 337 nm and

B) far UV-CD signal at 207 nm. The solid line represents the best fit calculated using Eq 4. C) Urea-induced unfolding transition of NbE201 normalized using Eq 5 (Material and Methods, section 5.6). Unfolded fraction curve relative to: the far UV-CD signal (●), the lambda max signal (▲), and the fluorescence intensity at 337 nm (■). D) Heat-induced unfolding transitions of NbE201 normalized (using Eq 5) and monitored by far UV-CD (in black) and intrinsic fluorescence (in red). Each symbol indicates the transition for a different production lot: (▲) lot 1, (■) lot 2 and (●) lot 3, for a total of N=3 replicates. E) Histograms representing the effects of oxidation on the inhibitory activity of AAT and NbE201. The ratios of inhibitor:hNE used for each inhibitor are: 1:1 for AAT:hNE, and 4:1 and 2:1 for NbE201:hNE. Each bar represents a different time point in the experiment: 0-6-24 h after chemical modification. The experiment was carried out in duplicate, n=2. F) Thermodynamic parameters of unfolding of NbE201 at pH 7.0, 25°C, as obtained from the analysis of the urea-induced equilibrium transitions. Data were fitted using Eq 4. Errors for $\Delta G^{\circ}_{NU(H2O)}$ and m_{NU} are derived from the fitting. C_m error was calculated using Eq 6.

Stability of NbE201 towards heat-induced denaturation. The stability of NbE201 towards heat-induced unfolding was assessed by measuring the signal at 206 nm by far-UV CD during the heating of the protein sample from 25 to 97°C at a of 0.5°C · min^{-1} heating rate and a cooling-down to 25°C at the same rate. The denaturation experiment was carried out with three NbE201 samples from three independent lots of production (Figure 5D, in black). A single transition was obtained suggesting that the secondary structures unfold cooperatively following a two-state model (N↔U). The refolding of NbE201 after heat-induced denaturation was also monitored (Figure SI10). The refolding was partial, thus only the apparent temperature of unfolding (T_m^{app}, temperature at which 50 % of the molecules are unfolded while the others are in the native state) was considered and the functional

reversibility was not investigated. The T_m^{app} was calculated for the transition obtained for three different lots of VHHs in the far-UV CD and two different lots of VHH in the intrinsic fluorescence and then averaged, it is 71.4 ± 1.4 °C.

Stability towards oxidation and deamidation. The stability of NbE201 towards oxidation and deamidation was investigated and compared to that of AAT. Both NbE201 and AAT were incubated under conditions promoting either oxidation or deamidation, and an aliquot was taken at different time points (i.e., 0, 6 and 24 h) and their ability to inhibit hNE was measured. At a ratio AAT:hNE=1:1, AAT already loses most of its inhibitory activity on hNE after 6 h (i.e., around 75% of the inhibitory activity is lost), while at 24 h, AAT loses 97% of its inhibitory activity (Figure 5E). On the other hand, NbE201 at ratio 4:1=NbE201:hNE keeps its full inhibitory activity even after 24 h of incubation in oxidizing conditions. When NbE201 is incubated with hNE at a ratio 2:1=NbE201:hNE, conditions under which activity loss of NbE201 will be more visible as shown in Figure 1A, a small loss in inhibitory potency (i.e., 7 %) is observed. This loss is, however, small compared to that observed for AAT.

The results for deamidation at different time points are illustrated in Figure SI11. In this case, deamidation, has a very limited effect on the inhibitory activity of both AAT and NbE201.

3 DISCUSSION

In a number of pathological conditions, hNE activity exceeds the inhibitory capacity of its endogenous inhibitors and this is associated to a range of detrimental effects in a large range of diseases such as: chronic wounds[6,7], cancer metastasis[8,9], cardiovascular diseases[10], IBDs[12–14] and lung diseases (e.g., CF & COPD)[4,15,17,43]. Human NE constitutes, therefore, a therapeutic target in these conditions and the therapeutic potential of elastase inhibition has been

validated in preclinical and clinical studies[4,20,44,45]. Despite large effort to find hNE inhibitors, only two molecules are in clinical use for a small number of diseases in a limited number of countries; i.e., AAT for the treatment of AAT-deficiency, and Sivelestat for ARDS and ALI. The main challenges for the successful clinical use include potency, selectivity and metabolic stability under physiological conditions[18].

In this work, we use a range of enzymatic and biophysical approaches to characterize in detail the *in vitro* properties of an inhibitory VHH, NbE201, including its inhibitory capacity and mechanism of inhibition, affinity, specificity and stability.

3.1 NbE201 is a very potent inhibitor of human and murine NE

NbE201 acts as a tight inhibitor of hNE with a K_i in the low nM range which is about 50 times lower than the K_i reported for Sivelestat (K_i = 200 nM)[46] although in experimental conditions differ in pH and temperature in both studies. Considering the IC_{50} values determined in this work for the hydrolysis of N-Succinyl-Ala-Ala-Ala-paraNitroAnilide, the potency of NbE201 is on average 0.6 and 1.9 that of AAT and Sivelestat, respectively. Moreover, for the hydrolysis of elastin, an endogenous substrate of hNE, the IC_{50} for NbE201 is 4 times higher than that AAT but it is 14 times lower than Sivelestat. The higher inhibition of AAT is due to its femtomolar affinity[39]. The inhibitory effect of Sivelestat is significantly reduced compared to what was observed for the hydrolysis of the small substrate. This is likely due to the experimental conditions. Indeed, in addition to the enzyme and substrate concentrations and the K_m (see Eq SI1), the IC_{50} also depends on the stability of the inhibitor during the experiment. The hydrolysis of elastin was carried out over 16 h and Sivelestat is likely unstable under these conditions.

NbE201 is the most potent antibody fragment inhibiting hNE described so far. The inhibitory fragments VH 1D1.43, Fab 1C10 and their respective IgGs, described by Chu et al. in 2021[29], exhibit IC_{50} values 47 to 1567 times higher than that of NbE201. Moreover, contrary to NbE201, none of these antibodies bind into the active site of the enzyme. Indeed, the epitopes of IgG1 1C10 and Fab 1C10 are located at the opposite side of the active site of hNE, likely acting by inducing a conformational change in the enzyme active site. The epitope of IgG 1D1.43 and the derived VH 1D1.43 is adjacent to the substrate binding site suggesting that their inhibitory effect result from steric hindrance[29].

3.2 NbE201 acts as a competitive inhibitor

NbE201 competes with hNE inhibitors known to bind in the active site of hNE suggesting that it acts as a competitive inhibitor. NbE201 is not hydrolyzed by hNE even upon prolonged incubation suggesting either that it does not bind into the active site in a substrate-like manner or that it binds in a substrate-like manner but it is resistant to hydrolysis. The X-ray crystal structure of the NbE201:hNE complex at 2.3 Å allowed to better understand the molecular basis of both the high inhibitory potency and specificity of NbE201. Note that the nomenclature of Schechter and Berger is used to describe the specific sites of protease-inhibitor interaction[47]. CDR1 and CDR3 of NbE201 accounts for most of the binding surface and make multiple contacts with the substrate binding pocket and surrounding loops (Figure 6). Out of the three CDRs of NbE201, the CDR3 is the one going the deepest in the pocket and therefore closest to the active site (Figure 6 and Figure 7B,D), whereas CDR1 stays more uplifted (Figure 7B,D). This mode of binding differs from those of previously proposed for several hNE protein inhibitors including SLPI (endogenous inhibitor), OMTKY3, EapH1 and ecotin (Figure 7A,C)[48–51]. For all of these, a continuous sequence of amino acids binds, deeper

into the active pocket, to S1-S2 and S1'-S2' subsites in a very similar manner. Ecotin, for example, binds in a substrate-like non covalent manner to hNE[51], inactivating the enzyme by its tight binding with the active site residues of hNE which disrupts the critical interactions of the active site Ser195 and other key residues, such as His57 and Gly193. An optimal hydrolysis-competent positioning was observed for the CDR3 of Nb4, a VHH inhibiting the trypsin-like urokinase-type plasminogen activator (uPA)[34] (Figure SI12B1,2). In fact, Nb4 can be hydrolysed by uPA because its scissile bond (P1-P1' as R110-R111) orientation in the uPA substrate pocket is in the direction from N-terminal to C-terminal (Figure SI12B1,2). This directionality allows the peptide bond hydrolysis to be completed once the reaction is started (i.e. following the initial nucleophilic attack by the active serine). Moreover, the scissile bond is at a distance of the hydroxyl group of S195 (i.e., 2.8 Å) that allows its nucleophilic attack. Nb4 can, however, resist hydrolysis due to its high stability associated with an intra-CDR3 dense hydrogen bond network[34]. As consequence, Nb4 can behave both as an inhibitor and as a poor substrate for this serine protease. Several conventional antibodies inhibiting the serine protease matriptase bind into the active site in a reversed C- to N- orientation which places the scissile bond out of reach of a nucleophilic attack from S195[52,53]. For NbE201, the bond that could correspond for its interactions with the substrate pocket to the scissile bond is the peptide bond between K101-L102. This peptide bond has not, however, the classical orientation in the S1-S1' pocket; it adopts instead a more perpendicular orientation (Figure SI12A1,2). Moreover, it is too distant from S195 (7.6 Å) to allow the nucleophilic attack by the catalytic serine 195 O^{γ} (i.e., ~2.7 Å optimal distance) (Figure SI12A1). This explains why NbE201 is a very potent inhibitor of hNE.

3.3 NbE201 is specific for hNE

NbE201 does not significantly inhibit the closely related serine proteases: hPR3, hCG and pPE. Such a high selectivity was also observed for VHHs inhibiting other enzymes including β-lactamases[54], lysozyme[55] and proteases[34,35]. NbE201 makes numerous interactions with the substrate binding pocket and surface loops surrounding it (Figure 6A,B). These loops contribute to the substrate specificity and therefore are sites of great diversity among the proteases from chymotrypsin-like proteases. The specificity of NbE201, therefore, likely results from its binding to both the substrate pocket and the surrounding loops.

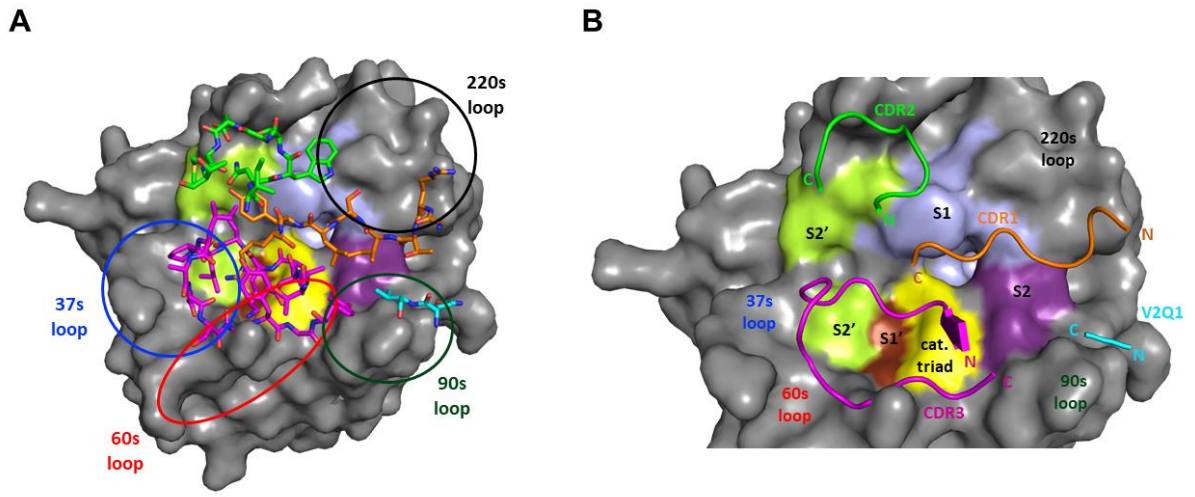

Figure 6. **NbE201 interacts with specificity loops of hNE and CDRs occupancy in the substrate pocket**. A) hNE surface loops and interacting amino acids of NbE201. The interacting amino acids of NbE201 are represented as sticks. B) CDRs of NbE201 occupancy in the substrate pocket of hNE. CDRs of NbE201 are represented as cartoons. A,B) hNE is shown as a grey surface and the substrate pockets are highlighted in different colours: S1 in light blue, S1' in brown, S2 in violet and S2' in lime green. The catalytic triad is in yellow. CDR1 is in orange, CDR2 is in light green and CDR3 is in magenta and the residues from FR1 are in light blue. Loop 37s (blue), residues 34–41; Loop 60s (red), residues 56–64; Loop 90s (dark green), residues 97–103; Loop 220s (black), residues 217–225.

NbE201 also acts as a tight binding inhibitor for mNE, although K_i is about 10 times higher than that for hNE. This is not surprising since it shares about 77% of sequence identity with hNE and especially since 60% of the residues making the epitope are conserved (Figure SI13). Its efficient cross reactivity with mNE makes NbE201 an unique tool for research in *in vivo* models.

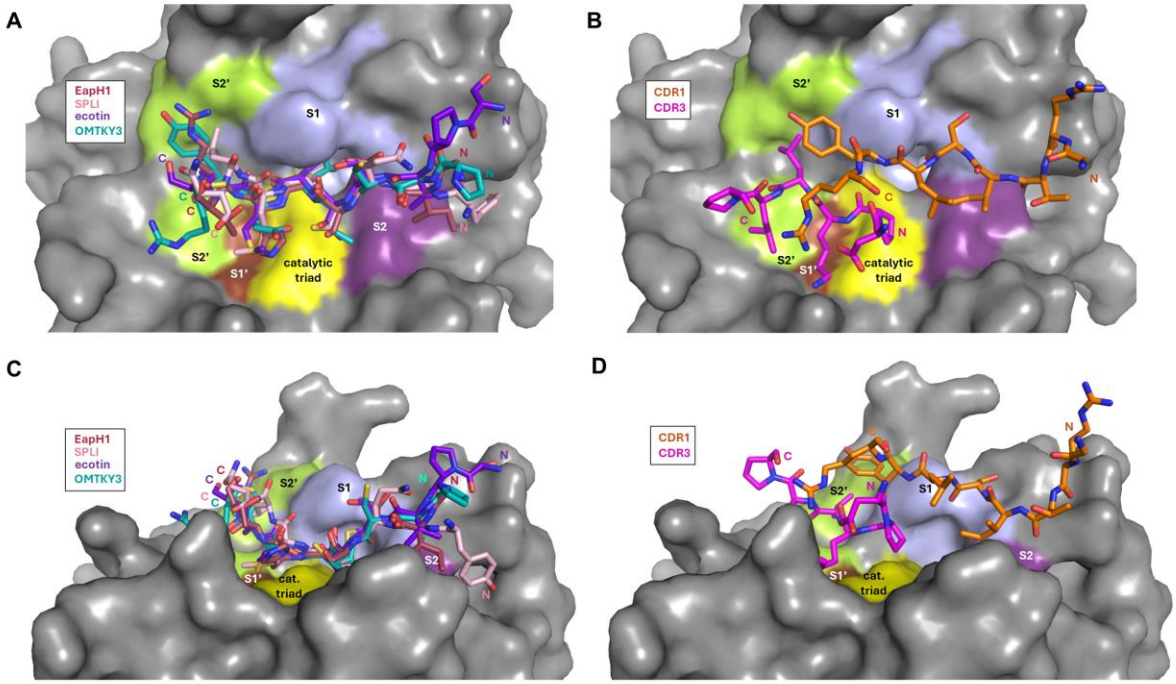

Figure 7. **Differences in the enzyme pocket occupation between NbE201 and the other protein inhibitors (OMTKY3, SPLI, EapH1 and ecotin)**. The pockets are highlighted in different colours: S1 in light blue, S1' in brown, S2 in violet and S2' in lime green. The catalytic triad is in yellow. The different paratopes of the protein inhibitors interacting with the enzyme pocket are depicted as sticks: NbE201 G26-R33 of CDR1 (orange) and D99-P104 of CDR3 (magenta), OMTKY3 (teal), SPLI (light pink), EapH1 (maroon) and ecotin (purple). Pannels A,C and B,D show respectively: A,C) Ecotin, SLPI, OMTKY3, EapH1 and B,D) NbE201.

3.4 NbE201 has a favourable development potential

To investigate the development potential of NbE201, we studied its stability towards chemical and heat-induced denaturation and towards oxidation and deamidation. Upon chemical denaturation, NbE201 unfolds cooperatively and reversibly following a single two-state transition, where only the native and unfolded states are populated without the formation of a significant amount of intermediate species. Such cooperative unfolding is generally observed for VHHs[37]. NbE201 exhibits a high conformational stability with a C_m of 5.9 ± 0.1 M urea, and a value of $\Delta G^{\circ}_{NU(H2O)}$ (41 ± 3 kJ mol^{-1}) in the upper range of that observed for other VHHs[37]. The heat-induced unfolding of NbE201 is also cooperative following a single two-state transition; the refolding upon cooling down is, however, only partial. The VHH starts to unfold at about 60°C, and the average apparent temperature of mid-transition (i.e. 71.4 ± 1.4 °C) is in the higher range of the T_ms observed for VHHs[37]. In order to improve their *in vivo* pharmacokinetics and pharmacodynamics, biologics including antibodies should often be further modified either by chemical or genetic engineering[56]. For example, given their small size, the half-life of VHHs following intravenous injection or inhalation is limited, and several strategies have been used to increase their half-lives including site-specific PEGylation[57]. Moreover, despite the low immunogenicity of VHHs[58], the use of NbE201 to treat chronic diseases will imply repeated administrations and it might therefore require the humanization of NbE201 in order to prevent the development of immune response. Such modifications can negatively affect the stability of the therapeutic proteins[59] and therefore it is important that the unmodified protein exhibits a high stability. Due to its high thermodynamic stability, NbE201 should tolerate conditions of manufacturing processes characterizing drug development and it is therefore an important feature for its developability.

In vitro, AAT is inactivated by exogenous oxidants (e.g., cigarette smoke) and endogenous oxidants from (e.g., neutrophil myeloperoxidase released at inflammatory sites)[60,61]. Thus,

the *in vivo* oxidation of AAT is likely to contribute to the development of inflammatory diseases. As previously reported[62], we observed that AAT rapidly loses its inhibitory capacity when incubated *in vitro* in oxidizing conditions (i.e., 70 % of the inhibitory capacity is lost in 6 h) while under similar conditions, the inhibitory capacity of NbE201 is only marginally altered after 24 h. The inhibitory capacity of NbE201, as that of AAT, is little affected under deamidation conditions. The high stability of NbE201 towards oxidation suggests an *in vivo* efficiency potentially higher than that of AAT, further highlighting its promising therapeutic potential.

4 CONCLUSIONS AND FUTURE PERSPECTIVES

NbE201, the first inhibitory VHH targeting hNE reported so far, was thoroughly characterized. This VHH acts as a tight, specific and competitive inhibitor of the enzyme. Its high inhibitory potency combined to its high thermodynamic and chemical stability make NbE201 a promising pharmacological tool to treat diseases associated with unregulated release of NE by neutrophils. Investigation of its pharmacokinetics and its inhibitory activity in disease relevant samples as well as *in vivo* models will constitute the object of future work. Moreover, NbE201 also constitutes a unique tool for prognostic purposes. Indeed, several studies on sputa from CF patients with chronic lung infections show that the concentration of active NE is higher than in normal controls subjects and that the majority of the enzyme is not complexed with the inhibitor AAT[63]. Active NE concentration in sputa is also directly correlated with the index severity in people suffering from bronchiectasis[64] and its concentration can be used to predict the next patients' exacerbation[65]. Several kits exist to quantify the concentration of active (i.e., free) hNE content in samples but they all, except

one (NEATstick, from ProAxis, which is a semi-quantitative point of care (POC) diagnostic device) need analysis in a laboratory. A quantitative POC diagnostic device is missing, that is a system that could be easy to use by the patient himself. NbE201 constitutes a unique tool for developing such an approach as well as for imaging active hNE.

5 MATERIAL AND METHODS

5.1 Production and purification of NbE201 and cAb-H7S-Nter-P1

The selection of NbE201 from an immune gene library of VHHs following the immunization of a llama with hNE will be described elsewhere (*Morales-Yánez et al., in preparation*). The gene coding for NbE201 was cloned into the pHEN6 vector using PstI and BstEII restriction sites and used to transform chemo-competent *E. coli* WK6 cells. The transformed cells were plated on LB-agar containing ampicillin (100 $mg{\cdot}L^{-1}$). One colony was picked to carry out a pre-culture in 100 mL of LB medium supplemented with ampicillin (100 $mg{\cdot}L^{-1}$), overnight at 37°C with orbital agitation (250 rpm). The preculture (5 mL) was used to inoculate 500 mL of Terrific Broth (TB) medium supplemented with glucose (0.1% v/v) and ampicillin (100 $mg{\cdot}L^{-1}$). The bacterial growth was performed at 37°C until the absorbance at 600_{nm} was comprised between 2 and 3. Then, 1 mM IPTG (final concentration) was added, and the culture was continued overnight at 28°C with orbital agitation. The cells were harvested by centrifugation (15 min at 4500 g) and the periplasmic extract was prepared by osmotic shock as described previously[66]. The periplasmic extract was then filtered through a 0.45 µm cut-off membrane and loaded in on a 5 mL IMAC NiPDC resin (Affilland, Liège, Belgium). The resin was washed with 50 mM imidazole in potassium phosphate (KPi) buffer 50 mM pH 8.0 and the VHH was eluted using 375 mM imidazole in KPi buffer 50 mM pH 8.0. The imidazole was removed using a 30

mL G25 Sephadex column (Sigma Aldrich) and 50 mM sodium phosphate (NaPi) buffer pH 7.0 as running buffer. The purity and the integrity of the VHH was verified by Coomassie-stained SDS-PAGE and mass spectroscopy (ESI-Q-TOF). The NbE201 concentration was determined by UV absorption at 280 nm using the theoretical extinction coefficient calculated from the amino-acid sequence using Expasy ProtParam tool.

cAb-H7S-Nter-P1 is a chimeric VHH consisting in the peptide P1 fused by a linker (GGGGS)x2 at the N-ter of the VHH cAb-H7S which is specific to the β-lactamase BlaP and therefore, it does not bind to hNE. P1 is composed by the inhibitory peptide sequence (β-hairpin) plus the β-stranded stalk derived from the bovine antibody BLV1H12[42]. The sequence of P1 is: TSVHQETKKMC*TASIPPQC*YYNYEWHVDV, where C*-C* indicates a disulphide bridge; the sequence of the inhibitory peptide is underlined. cAb-H7S-Nter-P1 was produced and purified following the protocol described above for NbE201.

5.2 Inhibition of hNE activity

Inhibition of the hydrolysis of a small chromogenic substrate. To determine the inhibitory capacity of NbE201, the hNE residual activity in the presence of the VHH at different VHH:hNE ratios was measured for the hydrolysis of N-Succinyl-Ala-Ala-Ala-paraNitroAnilide. Briefly, hNE (Elastin products company, EPC, United States) was resuspended at 1 $mg \cdot mL^{-1}$ in 50 mM sodium acetate buffer pH 5.0 containing 100 mM NaCl and stored at 4°C. The substrate N-Succinyl-Ala-Ala-Ala-paraNitroAnilide (1 mM) was dissolved in 0.1 M Tris pH 7.5 with 0.5 M NaCl and 0.01% (%w/v) NaN_3 and stored at 4°C. 230 µL of substrate (1 mM) were mixed with 10 µL of Bovine Serum Albumin 9 µM (BSA, Sigma-Aldrich, Germany; final concentration, C_f = 346 nM) and incubated 20 min at 25°C in a clear flat bottom 96-well plate (Greiner Bio-One, Belgium). Then, NbE201 was added at final concentrations of 0, 10, 20, 30, 40, 50, 60, 70, 80,

90, 100, 125, 150 and 200 nM. Immediately after, the hNE was added to the mix at a final concentration of 50 nM. The absorbance at 410 nm was measured every min for 60 min in a SpectraMax M2e Microplates Reader (Molecular Devices, California, USA). The initial velocity (v_i) determined in the presence of the VHH at different VHH:hNE ratios was compared to that measured in the absence of the VHH (v_0) to determine the residual activity. The deadtime between the addition of hNE and the first measurement was about 100 s. All experiments were performed in triplicate. In some experiments, the VHH was preincubated for 15 min with the hNE and the complex was added to the substrate. The same set-up without pre-incubation was used to determine the inhibitory capacity of two other inhibitors of hNE: AAT (Sigma-Aldrich, Germany) and Sivelestat (R&D systems, United Kingdom).

The IC_{50} was determined by considering the concentration of inhibitor at which the residual activity of the protease is 50%. The inhibition curve was fitted using SigmaPlot to derive the IC_{50} using an Exponential Decay, Single, 3 Parameter equation: f = y0+a*exp(-b*x).

Some hNE activity measurements, in the absence and the presence of NbE201, were also carried out in quartz microcuvette. The substrate N-Succinyl-Ala-Ala-Ala-paraNitroAnilide 1 mM was incubated at 25°C for 20 min; then, NbE201 was added at two different concentrations (C_f = 40 nM and 75 nM), as well as hNE (C_f = 50 nM). The hNE activity was monitored at 410 nm for 10 min using the spectrophotometer Specord 50 Plus (Analytik Jena) and data were collected with the WinAspectPlus software. Measurements were carried out in the presence of BSA (C_f = 346 nM). The deadtime between the addition of hNE and the first measurement was about 15 s.

Inhibition of the hydrolysis of elastin, a natural substrate of hNE. The hNE residual activity was measured in the presence of Elastin-CongoRed (Sigma Aldrich, Germany). hNE (132 nM)

was incubated with a solution of Elastin-CongoRed (10 $mg \cdot mL^{-1}$ in 0.1 M Tris pH 7.5, 0.5 M NaCl and 0.01%, %w/v NaN_3) and with different concentrations of NbE201 or of other inhibitors (AAT and Sivelestat). The samples were incubated for 16 h at 37°C with orbital shaking (900 rpm). The samples were then centrifuged at 90000 g for 30 min at 4°C to separate the insoluble elastin from the digested and soluble fragments. The soluble fraction was transferred into a 384-wells clear plate and the absorbance of CongoRed was measured at 495 nm in a SpectraMax M2e Microplates Reader. The absorbance of the samples at different inhibitor:hNE ratios was compared to that measured for hNE alone to determine the residual hNE activity. A sample of Elastin-CongoRed without elastase was used as blank. The experiment was performed in triplicate. The inhibition curve was fitted using SigmaPlot to derive the IC_{50} using an Exponential Decay, Single, 3 Parameter equation: f = y0+a*exp(-b*x).

5.3 Specificity of NbE201 for hNE

To determine whether NbE201 was specific for hNE, we first investigated its ability to inhibit several serine proteases: porcine pancreatic elastase (pPE, from Sigma), murine neutrophil elastase (mNE, from EPC) and with two other human serine proteases present in the lung: human neutrophil proteinase 3 (hPR3 from EPC) and human neutrophil cathepsin G (hCG from Calbiochem). The substrates used were N-Succinyl-Ala-Ala-Ala-paraNitroAnilide (1 mM in 0.1 M Tris pH 7.5 with 0.5 M NaCl and 0.01% (%w/v) NaN_3 from Sigma-Aldrich) for pPE, MeOSuc-Ala-Ala-Pro-Val-AMC (100 µM in Tris 50 mM pH 7.5, 1 M NaCl, 0.05% (%w/v) Brij-35,) for mNE, N-Succinyl-Ala-Ala-Pro-Phe p-nitroanilide (0.45 mM in 100 mM HEPES pH 7.5, from Sigma Aldrich) for hCG and Boc-Ala-Ala-Nva-SBzl (0.22 mM in in 100 mM MOPS pH 5.0 0.5 M NaCl, 100 µM DTNB, 10% (%v/v) DMSO from EPC) for hPR3. mNE (rmELA2 from R&D systems, United Kingdom) was first activated according to the supplier information. In brief, mNE was

incubated with recombinant mouse active cathepsin C/DPP-I (rmCathepsin C from R&D systems) in 50 mM MES, 50 mM NaCl, pH 5.5 for 2 h at 37°C. The enzyme concentrations in the assay were 6 nM, 14.7 nM, 25 nM, 5 nM for pPE, mNE, hCG and hPR3, respectively. Different molar ratios of NbE201:proteases were tested. The hydrolysis of the substrate and the determination of the residual activity were carried out as explained above for the inhibition of hNE.

The specificity of NbE201 was also investigated by Biolayer Interferometry (BLI) with the Octet HTX machine (Sartorius, Germany) of the Robotein platform of the Centre for Protein Engineering (CIP). Biotinylated NbE201 (10 $\mu g \cdot mL^{-1}$) was immobilized on streptavidin biosensors (SA, Sartorius) following the provider's indications. The biotinylation of NbE201 was performed on lysines using EZ-Link™ NHS-Biotin from ThermoFisher Scientific, for 30 min at RT with a ration Biotin/Nb = 2:1, following the provider's indications and the excess of biotin was removed by gel filtration using a 1 mL Hi-trap G25 column (Sigma Aldrich). The biosensors were then immersed in a 50 nM solution of a serine protease. The proteases tested were hCG, hPR3, mPE, mNE and pPE. hNE was used as a positive control. The association was measured for 70 s in kinetic buffer (KB, Sartorius). The experiments were carried out at 30°C in 384-wells black-bottom polypropylene microplates (Greiner Bio-One, Belgium) and with orbital agitation (1000 rpm).

5.4 Determination of the affinity of NbE201 for hNE and mNE by BLI experiments

The affinity of NbE201 for hNE and mNE (FigureSI5B) was measured by BLI with the Octet HTX machine using various settings. NbE201 was produced in the pHEN25 vector and was site-specifically biotinylated on its C-terminal Cys using EZ-Link Maleimide-PEG2-Biotin (ThermoFisher) and Tris(2-carboxyethyl)phosphine, immobilized on Agarose CL-4B (Sigma-

Aldrich), incubated for 2 h 30 min at RT in agitation in 50 mM NaPi buffer pH 7.0, 2 mM EDTA; the excess was removed by gel filtration. For hNE, the biotinylated NbE201 (0.5 µg·mL^{-1}) was immobilized on streptavidin biosensors (SA, Sartorius) following the provider's indications. Then, the biosensors were immersed in a solution of hNE at different concentrations (25 – 6.25 – 3.12 – 1.56 – 0.75 nM). Association and dissociation kinetics were measured for 180 s and 300 s respectively, in 10X KB buffer. For mNE, see experimental conditions in supplementary information section (Figure SI5B). All the experiments were carried out at 30°C in 96-wells or 384-wells black-bottom microplates in polypropylene (Greiner Bio-One, Belgium) and with orbital agitation (1500 rpm). Otherwise stated, the sensorgrams obtained were fitted globally to a 1:1 model to derive the k_{on} and k_{off} and the K_D. Three independent replicates were carried out for both hNE and mNE. The error on K_D was calculated using the Eq 3:

$$\sigma_{K_D} = \sqrt{\left(\frac{\sigma_{k_{off}}}{k_{off}}\right)^2 + \left(\frac{\sigma_{k_{on}}}{k_{on}}\right)^2} \cdot K_D \qquad \text{(Eq 3)}$$

where σ is the error, K_D is the dissociation constant at the equilibrium, k_{off} is the dissociation constant and k_{on} is the association constant.

5.5 Competitive binding of NbE201 with AAT, MeOSuc-Ala-Ala-Pro-Val-CMK and cAb-H7S-Nter-P1

Competitive binding assays between NbE201 and hNE in complex with either (i) AAT, (ii) MeOSuc-Ala-Ala-Pro-Val-CMK and (iii) cAb-H7S-Nter-P1 were also carried out by BLI with the Octet HTX equipment. NbE201 biotinylated on lysines (10 µg·mL^{-1} in KB buffer) was immobilized on SA biosensors following the provider's indications. A biosensor quenching

step with biocytin 1 µg·mL^{-1} was performed. Then, the biosensors were immersed in a 250 nM hNE solution pre-incubated with or without saturating concentrations of one active site competitors (1.5 µM AAT, 15 µM MeOSuc-Ala-Ala-Pro-Val-CMK or 1.5 µM cAb-H7S-Nter-P1). The association was measured for 280 s in KB buffer. The experiments were carried out at 30°C in 384-wells black-bottom polypropylene microplates (Greiner Bio-One, Belgium) and with agitation (1000 rpm).

5.6 Thermodynamic stability of NbE201

***Preparation of the samples*.** Samples of NbE201 were incubated overnight at 25°C in the presence of increasing concentrations of urea (Sigma-Aldrich) in 50 mM NaPi buffer pH 7.0. The protein concentration was 0.2 mg·mL^{-1}. The denaturant concentration in each sample was determined from refractive index measurements[67], using a R5000 hand refractometer from Atago (Tokyo, Japan). The same samples were used to measure both the intrinsic fluorescence and far UV-CD spectra. Blank samples (without the VHH) at each urea concentration were prepared to build a reference curve that was used to correct the contribution of (buffer + urea) to fluorescence and CD signals at each urea concentration. To check if, after denaturation in urea and renaturation, NbE201 recover its structure and biological activity (i.e., inhibition of hNE), NbE201 was incubated at 2 mg/mL in the absence or in the presence of 7.6 M urea for 1 h at 25°C. Each sample was then diluted at 0.2 mg/mL in NaPi buffer 50 mM pH 7.0 at different concentrations of urea and incubated overnight at 25°C. The spectra of intrinsic fluorescence of both series of samples were compared to establish the structural reversibility. Moreover, a hNE enzymatic assay was performed, as described above, with the two samples in 0.76 M urea (i.e. one from the unfolding/refolding

starting from 7.6 M urea and the other from none-denatured sample), to demonstrate the functional reversibility.

Measurements of fluorescence and far-UV-CD signals/spectra. Intrinsic fluorescence spectra to monitor changes in the tertiary structure were recorded at 25°C from 305 nm to 440 nm after excitation at 280 nm with 5 nm excitation and emission slits using a Cary Eclipse Fluorimeter (Agilent, Santa Clara, USA) equipped with a Peltier multi-cell holder and a 10*0.4 mm pathlength quartz micro cuvette. The voltage applied at the detector was 710 V. Data acquisition was made every 0.5 nm with a scan rate of 30 $nm \cdot min^{-1}$.

Far UV-CD spectrum of the native and denatured states (i.e., in 9 M urea) were recorded in a 0.2 mm pathlength quartz cuvette at 25°C. 4 spectra were accumulated. Each spectrum was recorded from 200 nm to 250 nm with a 0.1 nm data interval, 2 s integration time, a bandwidth of 1 nm and a scanning speed of 50 $nm \cdot min^{-1}$. The unfolding transitions were monitored by far UV-CD at 207 nm in a 0.2 mm pathlength quartz cuvette. At each denaturant concentration, 37 data points were acquired with a 1 nm bandwidth, a reading frequency of 5 s and a 4 s integration time, and averaged. The measurements were carried out with Jasco J-810 spectropolarimeter (JASCO, Lisses, France).

Data analysis. The intrinsic fluorescence spectra were fitted using a five parameter Weibull function (from software SigmaPlot 5.0) to determine the wavelength corresponding to the highest fluorescence intensity (λ_{max}). The changes in fluorescence intensity at 337 nm (i.e., a wavelength at which the fluorescence of the native and denatured proteins differ significantly as shown in Figure SI3), were also used to monitor the unfolding transition. The transition curves obtained, both by intrinsic fluorescence and far UV-CD, were analyzed based on a two-state (N ⇌ U) model according to Dumoulin *et al*.[37] and Eq 4:

$y_{obs} = \{(Y_N + p \bullet [x]) + (Y_U + q \bullet [x]) \bullet \exp(-a)\} / (1 + \exp(-a))$ (Eq 4)

where x is the concentration in denaturant and $a = (\Delta G^{\circ}_{NU(H2O)} - m_{NU} * [D])/RT$, and y_{obs} is the monitored signal (i.e. λ_{max}, F_{337nm} or CD_{207nm}) at a given denaturant concentration, and Y_N and Y_U are the values of these signals for the native and denatured states, respectively in the absence of denaturant. $\Delta G^{\circ}_{NU(H2O)}$ is the difference in free energy between the folded and unfolded states at 25°C; m_{NU} is a measure of the dependence of the free energy on the denaturant concentration, and [D] is the denaturant concentration. p and q are the slopes of the pre- and post-transition baselines, respectively, R is the gas constant, and T is the absolute temperature. C_m, the denaturant concentration at the midpoint of the denaturation curve ([U]/[N] = 1) is defined as $\Delta G^{\circ}_{NU(H2O)}/m_{NU}$.

The transitions were normalized using the Eq 5:

$y = \{y_{obs} - (Y_N + p \bullet [x])\} / \{(Y_U + q \bullet [x]) - (Y_N + p \bullet [x])\}$ (Eq 5)

The error on C_m has been calculated using Eq 6:

$$\sigma_{C_m} = \sqrt{\left(\frac{\sigma_{\Delta G}}{\Delta G}\right)^2 + \left(\frac{\sigma_{m_{NU}}}{m_{NU}}\right)^2} \cdot C_m \qquad \text{(Eq 6)}$$

where σ is the error, ΔG is is the difference in free energy between the folded and unfolded states, m_{NU} is a measure of the dependence of the free energy on the denaturant concentration and C_m is the denaturant concentration at the midpoint of the denaturation curve.

5.7 Thermal stability of NbE201

***Preparation of the samples and measurements*.** Samples of NbE201 in 50 mM NaPi buffer pH 7.0 were prepared at a protein concentration of 0.2 $mg \cdot mL^{-1}$. All the experiments were carried

out in 1 mm quartz cell and a JASCO J-810 CD spectrophotometer equipped with a Peltier cell-holder. Mineral oil was added on the top of the samples to avoid sample evaporation. The CD spectrum of the native and denatured states of the protein were recorded from 190 nm to 250 nm at 25°C and at 97°C, respectively with a 1 nm data interval, a data pitch of 0.1 nm, 2 s integration time, a bandwidth of 1 nm and a scanning speed of 50 $nm \cdot min^{-1}$. Heat-induced unfolding was monitored by far UV-CD at 206 nm (i.e., a wavelength at which the signals of the native and denatured state differ significantly). The temperature was increased linearly from 25 °C to 97°C at a heating rate of 0.5 $°C \cdot min^{-1}$, and data points were acquired every 0.3°C. The reversibility of the phenomenon (Figure SI9) was assayed by cooling the sample from 97°C to 25°C at the same rate. Data were acquired using a 4 s integration time and a 1 nm bandwidth. The temperature in the cell was monitor with the help of a thermocouple (PT200 differential thermometer, IMPOT Electronics, Albertslund, Denmark).

Data analysis. The transition curves obtained were analyzed based on a two-state (N ⇌ U) model according to *El Hajjaji et al*.[68] and Eq 4 where x is the absolute temperature and a = -(ΔH_m (1-x/T_m))/Rx, and y_{obs} is the CD signal at 206 nm at a given temperature (x), and Y_N and Y_U are the values of these signals for the native and denatured states, respectively at 273K. p and q are the slopes of the pre- and post-transition baselines, respectively, R is the gas constant. T_m is the temperature of mid-transition and ΔH_m is the enthalpy value at T_m. Since the transitions were not fully reversible, only the Tm which is referred to as apparent T_m (T_m^{app}), was considered. The transitions were normalized using the Eq 5.

5.8 Stability towards oxidation

Oxidizing conditions were obtained by diluting the samples (protein final concentration 0.5 $mg \cdot mL^{-1}$) with an equal volume of 0.1 % H_2O_2 (v/v) and incubation at room temperature. After

0 h, 6 h, and 24 h a 10 µL aliquot was taken and analyzed by an activity inhibition test as described previously.

5.9 Stability of NbE201 towards hNE

NbE201 (26.4 µM) was incubated at 37°C alone or in the presence of hNE ([NbE201]:[hNE]=4:1). Aliquots (10 µL) taken at different time intervals were mixed with 4 µL of sample loading buffer (Tris-HCl (pH 6.8), SDS denaturant (4%, %w/v), β-mercaptoethanol (5%, %v/v), bromophenol blue (0.01%, %w/v), glycerol (20%, %v/v), H_2O)) and then stored at -20°C until analysis by SDS-PAGE using 4–20% Mini-PROTEAN TGX Protein Gel, 10 wells, 50 µL (Bio-Rad, Germany). Then, the gel was stained by Coomassie blue, distained in water and imaged using a Gel Doc EZ Imager (Biorad). The relative amount of intact protein was quantified by densitometry analysis with a Gel Doc EZ Imager program using the intensity of the band at time zero as the relative standard. hNE alone was incubated under similar conditions and an aliquot was taken at different time points to measure its activity using N-Succinyl-Ala-Ala-Ala-paraNitroAnilide as substrate as described above.

5.10 Determination of the NbE201 structure alone and in complex with hNE

The crystals were grown at 20°C using the sitting drop vapor diffusion method. For NbE201 alone, the drop contained 0.2 µL of NbE201 at a concentration of 15 mg·mL^{-1} in PBS buffer (pH 7.4, 10 mM Na_2HPO_4, 1.8 mM KH_2PO4, 137 mM NaCl, 2.7 mM KCl) and 0.2 µL of precipitant solution (0.2 M Ca Acetate, 0. 1M Na Cacodylate pH 6.5 with 18% (%v/v) polyethylene glycol 8000). The complex for crystallization was formed by adding, in a molar ratio 1:1, the recombinantly produced and purified NbE201 to the lyophilized hNE, in order to have the final complex concentration of 15 mg·mL in PBS buffer. The solution obtained was used for crystallization without further purification. The drop allowing crystallization

contained 0.2 µL of protein solution and 0.2 µL of 0.1M HEPES pH 7.0 buffer with 10% (%v/v) polyethylene glycol 5000 monomethyl ether and 5% (%v/v) tacsimate. The crystals were transferred into a cryoprotectant solution containing 33% (%v/v) polyethylene glycol 6000 and 33% (%v/v) glycerol before being frozen in liquid nitrogen.

Data collection, phasing, model construction and refinement for both structures. Diffraction data were collected at the Proxima 1 and Proxima 2a beamlines of the Soleil synchrotron (Saint Aubin, France) for the NbE201:hNE complex and NbE201 alone, respectively. Indexing, integration and scaling of the data were carried out with the XDS Program Package[69]. The structure of hNE alone (PDB 3Q76) and the structure of the VHH specific of the mouse Vsig4 protein (PDB 5IMO) were used to obtain the initial phases of the complex NbE201:hNE by molecular replacement using the Phaser Crystallographic program[70]. The same program was used to obtain the initial phases of NbE201 by molecular replacement using the structure of the solved complex NbE201:hNE. The structures were built using the Coot program (Crystallographic Object-Oriented Toolkit)[71] and refined with BUSTER -TNT[72]. The amino acid numbering scheme was based on the chymotrypsin system. The surface of interaction of the complex was calculated with the PDBePISA server (https://www.ebi.ac.uk/pdbe/pisa/). The interactions were found using PyMOL and the RING plugin (https://ring.biocomputingup.it/). The figures were prepared using PyMOL software (The PyMOL Molecular Graphics System, Version 2.5.4 Enhanced for Mac OS X, Schrödinger, LLC.).

***Accession numbers*.** The PDB code for the structure of the complex and the free VHH are, respectively 8QGX and 8QGZ.

Figures

Figures were prepared with PyMOL (The PyMOL Molecular Graphics System, Version 2.5.4 Enhanced for Mac OS X, Schrödinger, LLC.), SigmaPlot (Version 5.0 Systat Software, Inc., San Jose, California) and GraphPad Prism 10.0 (GraphPad Software, Inc., San Diego, CA).

SUPPLEMENTARY MATERIAL DESCRIPTION

One file comprising 13 figures (FigureSI1-FigureSI13) with a description for every figure and additional information (material and methods, comments) for some figures, a table (TableSI1) and an equation (EqSI1).

ACKNOWLEDGEMENTS

We thank the Protein Factory Platform at Center for Protein Engineering for providing material necessary for protein purification of the VHHs. We acknowledge the Robotein® platform of the BE Instruct-ERIC Centre for providing access to the OctetHTX. We thank Alain Brans, Fabrice Bouillenne and Anne-Marie Matton for their support for the purification of the VHHs. We thank Marylène Vandevenne and Jean-Marie Frère for the critical reading of the manuscript. We thank Giovanni Minervini for the support during the analysis of the interactions *in silico*. This work was supported by a Walinnov project (Grant No. 1710173) from the Walloon Region. Paola Redeghieri is FRS-FNRS PhD fellow, FK & MD are research associate from the FRS-FNRS.

BIBLIOGRAPHY

1. Korkmaz B, Horwitz MS, Jenne DE, Gauthier F (2010) Neutrophil Elastase, Proteinase 3, and

Cathepsin G as Therapeutic Targets in Human Diseases Sibley D, editor. Pharmacol. Rev. 62:726–759.

2. Curciarello R, Sobande T, Jones S, Giuffrida P, Di Sabatino A, Docena GH, Macdonald TT, Kok K (2020) Human neutrophil elastase proteolytic activity in ulcerative colitis favors the loss of function of therapeutic monoclonal antibodies. J. Inflamm. Res. 13:233–243.

3. Bédard M, McClure CD, Schiller NL, Francoeur C, Cantin A, Denis M (1993) Release of Interleukin-8, Interleukin-6, and Colony-stimulating Factors by Upper Airway Epithelial Cells: Implications for Cystic Fibrosis. Am. J. Respir. Cell Mol. Biol. 9:455–462.

4. Twigg MS, Brockbank S, Lowry P, Fitzgerald SP, Taggart C, Weldon S (2015) The Role of Serine Proteases and Antiproteases in the Cystic Fibrosis Lung. Mediators Inflamm. 2015.

5. Ferry G, Lonchampt M, Pennel L, De Nanteuil G, Canet E, Tucker GC (1997) Activation of MMP-9 by neutrophil elastase in an in vivo model of acute lung injury. FEBS Lett. 402:111–115.

6. Ferreira A V., Perelshtein I, Perkas N, Gedanken A, Cunha J, Cavaco-Paulo A (2017) Detection of human neutrophil elastase (HNE) on wound dressings as marker of inflammation. Appl. Microbiol. Biotechnol. 101:1443–1454.

7. Grinnell F, Zhu M (1996) Fibronectin degradation in chronic wounds depends on the relative levels of elastase, α1-proteinase inhibitor, and α2-macroglobulin. J. Invest. Dermatol. 106:335–341.

8. Hu W, Lee SML, Bazhin A V., Guba M, Werner J, Nieß H (2023) Neutrophil extracellular traps facilitate cancer metastasis: cellular mechanisms and therapeutic strategies. J. Cancer Res. Clin. Oncol. 149:2191–2210.

9. Ho AS, Chen CH, Cheng CC, Wang CC, Lin HC, Luo TY, Lien GS, Chang J (2014) Neutrophil elastase as a diagnostic marker and therapeutic target in colorectal cancers. Oncotarget 5:473–480.

10. Glinzer A, Ma X, Prakash J, Kimm MA, Lohöfer F, Kosanke K, Pelisek J, Thon MP, Vorlova S, Heinze KG, et al. (2017) Targeting Elastase for Molecular Imaging of Early Atherosclerotic Lesions. Arterioscler. Thromb. Vasc. Biol. 37:525–533.

11. Zhukov AS, Khairutdinov VR, Samtsov A V., Krasavin M, Garabadzhiu A V. (2021) Preclinical efficacy investigation of human neutrophil elastase inhibitor sivelestat in animal model of psoriasis. Ski. Heal. Dis. 2:e90.

12. Chen KJ, Chen YL, Ueng SH, Hwang TL, Kuo LM, Hsieh PW (2021) Neutrophil elastase inhibitor (MPH-966) improves intestinal mucosal damage and gut microbiota in a mouse model of 5-fluorouracil–induced intestinal mucositis. Biomed. Pharmacother. 134:111152.

13. Barry R, Ruano-Gallego D, Radhakrishnan ST, Lovell S, Yu L, Kotik O, Glegola-Madejska I, Tate EW, Choudhary JS, Williams HRT, et al. (2020) Faecal neutrophil elastase-antiprotease balance reflects colitis severity. Mucosal Immunol. 13:322–333.

14. Edgington-Mitchell LE (2016) Pathophysiological roles of proteases in gastrointestinal disease. Am. J. Physiol. - Gastrointest. Liver Physiol. 310:G234–G239.

15. Rodrigues S de O, da Cunha CMC, Soares GMV, Silva PL, Silva AR, Gonçalves-De-albuquerque CF (2021) Mechanisms, pathophysiology and currently proposed treatments of chronic obstructive pulmonary disease. Pharmaceuticals 14:979.

16. Chalmers JD, Mall MA, Chotirmall SH, Donnell AEO, Flume PA, Ringshausen FC, Watz H, Xu J, Shteinberg M, Mcshane PJ (2024) Targeting neutrophil serine proteases in bronchiectasis.

Eur Respir J.

17. Guéant JL, Guéant-Rodriguez RM, Fromonot J, Oussalah A, Louis H, Chery C, Gette M, Gleye S, Callet J, Raso J, et al. (2021) Elastase and exacerbation of neutrophil innate immunity are involved in multi-visceral manifestations of COVID-19. Allergy Eur. J. Allergy Clin. Immunol. 76:1846–1858.

18. von Nussbaum F, Li VMJ (2015) Neutrophil elastase inhibitors for the treatment of (cardio)pulmonary diseases: Into clinical testing with pre-adaptive pharmacophores. Bioorg. Med. Chem. Lett. 25:4370–4381.

19. Mall MA, Davies JC, Donaldson SH, Jain R, Chalmers JD, Shteinberg M (2024) Neutrophil serine proteases in cystic fibrosis: role in disease pathogenesis and rationale as a therapeutic target. Eur. Respir. Rev. 33.

20. Matera MG, Rogliani P, Ora J, Calzetta L, Cazzola M (2023) A comprehensive overview of investigational elastase inhibitors for the treatment of acute respiratory distress syndrome. Expert Opin. Investig. Drugs 32:793–802.

21. Jin Z, Liu J-Y, Feng R, Ji L, Jin Z-L, Li H-B (2020) Drug treatment of coronavirus disease 2019 (COVID-19) in China. Eur. J. Pharmacol. 883:173326.

22. Zeiher BG, Artigas A, Vincent JL, Dmitrienko A, Jackson K, Thompson BT, Bernard G (2004) Neutrophil elastase inhibition in acute lung injury: Results of the STRIVE study. Crit. Care Med. 32:1695–1702.

23. Ding Q, Wang Y, Yang C, Li X, Yu X (2023) Clinical Utility of the Sivelestat for the Treatment of ALI/ARDS: Moving on in the Controversy? Intensive Care Res. 3:12–17.

24. U.S. Food and Drug Administration FDA Sivelestat. Available from:

https://www.accessdata.fda.gov/scripts/opdlisting/oopd/detailedIndex.cfm?cfgridkey=796020

25. Malicki S, Książek M, Sochaj Gregorczyk A, Kamińska M, Golda A, Chruścicka B, Mizgalska D, Potempa J, Marti H-P, Kozieł J, et al. (2023) Identification and characterization of aptameric inhibitors of human neutrophil elastase. J. Biol. Chem. 299:104889.

26. Holliger P, Hudson PJ (2005) Engineered antibody fragments and the rise of single domains. Nat. Biotechnol. 23:1126–1136.

27. Castelli MS, McGonigle P, Hornby PJ (2019) The pharmacology and therapeutic applications of monoclonal antibodies. Pharmacol. Res. Perspect. 7:e00535.

28. Davies PL, Maxwell NC, Kotecha S, Spiller OB (2008) Monoclonal anti-neutrophil elastase antibody characterisation: Ability to block function, detect free versus serpin-complexed enzyme and stain intracellular granules. J. Immunol. Methods 336:175–182.

29. Chu X, Sun Z, Baek DS, Li W, Mellors JW, Shapiro SD, Dimitrov DS (2021) Human antibody domains and fragments targeting neutrophil elastase as candidate therapeutics for cancer and inflammation-related diseases. Int. J. Mol. Sci. 22:11136.

30. Conrath KE, Lauwereys M, Galleni M, Matagne A, Frère JM, Kinne J, Wyns L, Muyldermans S (2001) Beta-lactamase inhibitors derived from single-domain antibody fragments elicited in the camelidae. Antimicrob. Agents Chemother. 45:2807–12.

31. Muyldermans S (2013) Nanobodies: Natural single-domain antibodies. Annu. Rev. Biochem. 82:775–797.

32. Pain C, Dumont J, Dumoulin M (2015) Camelid single-domain antibody fragments: Uses and prospects to investigate protein misfolding and aggregation, and to treat diseases

associated with these phenomena. Biochimie 111:82–106.

33. Armstrong LA, Lange SM, Cesare VD, Matthews SP, Nirujogi RS, Cole I, Hope A, Cunningham F, Toth R, Mukherjee R, et al. (2021) Biochemical characterization of protease activity of Nsp3 from SARS-CoV-2 and its inhibition by nanobodies. PLoS One 16:1–25.

34. Kromann-Hansen T, Oldenburg E, Yung KWY, Ghassabeh GH, Muyldermans S, Declerck PJ, Huang M, Andreasen PA, Ngo JCK (2016) A Camelid-derived Antibody Fragment Targeting the Active Site of a Serine Protease Balances between Inhibitor and Substrate Behavior. J. Biol. Chem. 291:15156–15168.

35. Razai AS, Eckelman BP, Salvesen GS (2020) Selective inhibition of matrix metalloproteinase 10 (MMP10) with a single-domain antibody. J. Biol. Chem. 295:646–3100.

36. de Marco A, Berrow N, Lebendiker M, Garcia-Alai M, Knauer SH, Lopez-Mendez B, Matagne A, Parret A, Remans K, Uebel S, et al. (2021) Quality control of protein reagents for the improvement of research data reproducibility. Nat. Commun. 12:2795.

37. Dumoulin M, Conrath K, Van Meirhaeghe A, Meersman F, Heremans K, Frenken LGJ, Muyldermans S, Wyns L, Matagne A (2002) Single-domain antibody fragments with high conformational stability. Protein Sci. 11:500–515.

38. Copeland R Enzymes: A Practical Introduction to Structure, Mechanism, and Data Analysis. Second edi. (Wiley-VHC, editor.). New York; 2000.

39. Tyagi SC (1991) Reversible inhibition of neutrophil elastase by thiol-modified α-1 protease inhibitor. J. Biol. Chem. 266:5279–5285.

40. Silverman GA, Bird PI, Carrell RW, Church FC, Coughlin PB, Gettins PGW, Irving JA, Lomas DA, Luke CJ, Moyer RW, et al. (2001) The Serpins Are an Expanding Superfamily of Structurally

Similar but Functionally Diverse Proteins. J. Biol. Chem. 276:33293–33296.

41. An-Zhi W, Mayr I, Bode W (1988) The refined 2.3 Å crystal structure of human leukocyte elastase in a complex with a valine chloromethyl ketone inhibitor. FEBS Lett. 234:367–373.

42. Liu T, Fu G, Luo X, Liu Y, Wang Y, Wang RE, Schultz PG, Wang F, T L, G F, et al. (2015) Rational design of antibody protease inhibitors. J. Am. Chem. Soc. 137:4042–4045.

43. Dicker AJ, Crichton ML, Pumphrey EG, Cassidy AJ, Suarez-Cuartin G, Sibila O, Furrie E, Fong CJ, Ibrahim W, Brady G, et al. (2018) Neutrophil extracellular traps are associated with disease severity and microbiota diversity in patients with chronic obstructive pulmonary disease. J. Allergy Clin. Immunol. 141:117–127.

44. Drury B, Hardisty G, Gray RD, Ho G tzer (2021) Neutrophil Extracellular Traps in Inflammatory Bowel Disease: Pathogenic Mechanisms and Clinical Translation. Cmgh 12:321–333.

45. Polverino E, Rosales-Mayor E, Dale GE, Dembowsky K, Torres A, Rosales-Mayor E, Dale GE, Dembowsky K, Torres A (2017) The Role of Neutrophil Elastase Inhibitors in Lung Diseases. Chest 152:249–262.

46. Kawabata K, Suzuki M, Sugitani M, Imaki K, Toda M, Miyamoto T (1991) ONO-5046, a novel inhibitor of human neutrophil elastase. Biochem. Biophys. Res. Commun. 177:814–820.

47. Schechter I, Berger A (1968) On the active site of proteases. III. Mapping the active site of papain; specific peptide inhibitors of papain. Biochem. Biophys. Res. Commun. 32:898–902.

48. Koizumi M, Fujino A, Fukushima K, Kamimura T, Takimoto-Kamimura M (2008) Complex of human neutrophil elastase with 1/2SLPI. J. Synchrotron Radiat. 15:308–311.

49. Bode W, Wei AZ, Huber R, Meyer E, Travis J, Neumann S (1986) X-ray crystal structure of the complex of human leukocyte elastase (PMN elastase) and the third domain of the turkey ovomucoid inhibitor. EMBO J. 5:2453–2458.

50. Gido CD, Herdendorf TJ, Geisbrecht B V. (2023) Characterization of two distinct neutrophil serine protease–binding modes within a Staphylococcus aureus innate immune evasion protein family. J. Biol. Chem. 299:102969.

51. Jobichen C, Prabhakar MT, Loh SN, Sivaraman J (2020) Structural Basis for the Inhibition Mechanism of Ecotin against Neutrophil Elastase by Targeting the Active Site and Secondary Binding Site. Biochemistry 59:2788–2795.

52. Schneider EL, Lee MS, Baharuddin A, Goetz DH, Farady CJ, Ward M, Wang CI, Craik CS (2012) A reverse binding motif that contributes to specific protease inhibition by antibodies. J. Mol. Biol. 415:699–715.

53. Farady CJ, Egea PF, Schneider EL, Darragh MR, Craik CS (2008) Structure of an Fab-Protease Complex Reveals a Highly Specific Non-canonical Mechanism of Inhibition. J. Mol. Biol. 380:351–360.

54. Cawez F, Mercuri PS, Morales-Yãnez FJ, Maalouf R, Vandevenne M, Kerff F, Guérin V, Mainil J, Thiry D, Saulmont M, et al. (2023) Development of Nanobodies as Theranostic Agents against CMY-2-Like Class C β-Lactamases. Antimicrob. Agents Chemother. 67:e0149922.

55. Desmyter A, Transue TR, Ghahroudi MA, Dao Thi M-H, Poortmans F, Hamers R, Muyldermans S, Wyns L (1996) Crystal structure of a camel single-domain VH antibody fragment in complex with lysozyme. Nat. Struct. Mol. Biol. 3:803–811.

56. Rondon A, Mahri S, Morales-Yanez F, Dumoulin M, Vanbever R (2021) Protein Engineering

Strategies for Improved Pharmacokinetics. Adv. Funct. Mater. 31:2101633.

57. Vugmeyster Y, Entrican CA, Joyce AP, Lawrence-Henderson RF, Leary BA, Mahoney CS, Patel HK, Raso SW, Olland SH, Hegen M, et al. (2012) Pharmacokinetic, biodistribution, and biophysical profiles of TNF nanobodies conjugated to linear or branched poly(ethylene glycol). Bioconjug. Chem. 23:1452–1462.

58. Ackaert C, Smiejkowska N, Xavier C, Sterckx YGJ, Denies S, Stijlemans B, Elkrim Y, Devoogdt N, Caveliers V, Lahoutte T, et al. (2021) Immunogenicity Risk Profile of Nanobodies. Front. Immunol. 12:632687.

59. Mahri S, Wilms T, Hagedorm P, Guichard MJ, Vanvarenberg K, Dumoulin M, Frijlink H, Vanbever R (2023) Nebulization of PEGylated recombinant human deoxyribonuclease I using vibrating membrane nebulizers: A technical feasibility study. Eur. J. Pharm. Sci. 189:106522.

60. Carp H, Janoff A (1979) In vitro suppression of serum elastase-inhibitory capacity by reactive oxygen species generated by phagocytosing polymorphonuclear leukocytes. J. Clin. Invest. 63:793–797.

61. Janoff A, Carp H, Lee DK Inactivation of alpha 1-proteinase inhibitor and bronchial mucous proteinase inhibitor by cigarette smoke in vitro and in vivo. In: Biochemistry, Pathology and Genetics of Pulmonary Emphysema. Elsevier; 1981. pp. 321–340.

62. Taggart C, Cervantes-Laurean D, Kim G, McElvaney NG, Wehr N, Moss J, Levine RL (2000) Oxidation of either Methionine 351 or Methionine 358 in α1-Antitrypsin Causes Loss of Anti-neutrophil Elastase Activity. J. Biol. Chem. 275:27258–27265.

63. Goldstein W, Doring G (1986) Lysosomal enzymes from polymorphonuclear leukocytes and proteinase inhibitors in patients with cystic fibrosis. Am. Rev. Respir. Dis. 134:49–56.

64. Gramegna A, Amati F, Terranova L, Sotgiu G, Tarsia P, Miglietta D, Calderazzo MA, Aliberti S, Blasi F (2017) Neutrophil elastase in bronchiectasis. Respir. Res. 18:1–13.

65. Keir HR, Fong CJ, Dicker AJ, Chalmers JD (2017) Profile of the ProAxsis active neutrophil elastase immunoassay for precision medicine in chronic respiratory disease. Expert Rev. Mol. Diagn. 17:875–884.

66. Skerra A, Plückthun A (1988) Assembly of a functional immunoglobulin Fv fragment in Escherichia coli. Science (80-.). 240:1038–1041.

67. Pace CN (1986) Determination and analysis of urea and guanidine hydrochloride denaturation curves. Methods Enzymol. 131:266–280.

68. Hajjaji H El, Dumoulin M, Matagne A, Colau D, Roos G, Messens J, Collet JF (2009) The zinc center influences the redox and thermodynamic properties of escherichia coli thioredoxin 2. J. Mol. Biol. 386:60–71.

69. Kabsch W, T. BA, K. D, A. KP, K. D, S. M, G. RRB, P. E, S. F, K. W, et al. (2010) XDS. Acta Crystallogr. Sect. D Biol. Crystallogr. 66:125–132.

70. McCoy AJ, Grosse-Kunstleve RW, Adams PD, Winn MD, Storoni LC, Read RJ (2007) Phaser crystallographic software. J. Appl. Crystallogr. 40:658–674.

71. Emsley P, Lohkamp B, Scott WG, Cowtan K (2010) Features and development of Coot. Acta Crystallogr. Sect. D Biol. Crystallogr. 66:486–501.

72. Blanc E, Roversi P, Vonrhein C, Flensburg C, Lea SM, Bricogne G (2004) Refinement of severely incomplete structures with maximum likelihood in BUSTER-TNT. Acta Crystallogr. Sect. D Biol. Crystallogr. 60:2210–2221.